minerals

IMPACT FACTOR 2.818

CITESCORE 3.7

Article

Hydrothermal Alteration Zones' Magnetic Susceptibility Footprints and 3D Model of Iron Oxide-Copper-Gold (IOCG) Mineralization, Carajás Mineral Province, Brazil

Marcelo Leão-Santos, Roberto Moraes, Yaoguo Li, Maria Irene Raposo and Boxin Zuo

Special Issue
Footprints of Mineral Systems

Edited by
Prof. Dr. Adalene Moreira Silva, Prof. Dr. Catarina Labouré Bemfica Toledo and
Prof. Dr. António Manuel Nunes Mateus

MDPI

https://doi.org/10.3390/min12121581

minerals

MDPI

Article

Hydrothermal Alteration Zones' Magnetic Susceptibility Footprints and 3D Model of Iron Oxide-Copper-Gold (IOCG) Mineralization, Carajás Mineral Province, Brazil

Marcelo Leão-Santos [1,2,*], Roberto Moraes [2,†], Yaoguo Li [3], Maria Irene Raposo [4] and Boxin Zuo [5]

[1] Faculty of Planaltina, University of Brasília, Brasília 73345-010, DF, Brazil
[2] Institute of Geosciences, University of Brasília, Brasília 70910-900, DF, Brazil
[3] Center for Gravity, Electrical and Magnetic Studies, Department of Geophysics, Colorado School of Mines, Golden, CO 80401, USA
[4] Institute of Geosciences, University of São Paulo, São Paulo 05508-080, SP, Brazil
[5] School of Computer Sciences, China University of Geosciences, Wuhan 430079, China
* Correspondence: marcelo.leao@unb.br
† In memoriam.

Abstract: Brownfield areas are important targets of exploration; however, the extensive drilling present in these areas has not fully exploited their prospective potential. The appropriate use of drill hole cores in these areas can play an important role in deep exploration. We present a case study of iron oxide-copper-gold (IOCG) Furnas Southeast deposit, located in the Carajás Mineral Province, Brazil. This deposit has disseminated chalcopyrite, bornite and gold mineralization associated with a silicic (Si), potassic (K), calcic (Na), sodic-calcic (Na-Ca) hydrothermal alteration, and intense iron metasomatism with massive magnetite (Fe) alteration. Petrophysical hand-held equipment measurements were carried out on drill core samples with the purpose of studying the potential roles that magnetic susceptibility properties can play in high-grade mineralization. The results indicate that the geological complexity of the IOCG deposit is readily reflected in the extensive variation of the measurements. The statistical analysis shows how the detailed characterization of this physical property carried out for this mineral association could effectively define and describe ore, and the magnetic susceptibility footprints of hydrothermal alteration zones. Furthermore, we were able to perform a magnetic susceptibility 3D modeling of diamagnetic, paramagnetic, and ferrimagnetic responses strictly correlated with known orebody. Thus, petrophysical analyses can form a quantitative geological criterion for ore delineation.

Keywords: petrophysics; magnetic susceptibility footprints; magnetite hydrothermal alterations; iron oxide-copper-gold (IOCG) mineralization; Carajás Mineral Province

Citation: Leão-Santos, M.; Moraes, R.; Li, Y.; Raposo, M.I.; Zuo, B. Hydrothermal Alteration Zones' Magnetic Susceptibility Footprints and 3D Model of Iron Oxide-Copper-Gold (IOCG) Mineralization, Carajás Mineral Province, Brazil. *Minerals* **2022**, *12*, 1581. https://doi.org/10.3390/min12121581

Academic Editor: Pei Ni

Received: 21 September 2022
Accepted: 6 December 2022
Published: 9 December 2022

1. Introduction

Target exploration in brownfield areas increases the probability of discovering new orebodies due to the extension of the geological fertile environment and an advantageously built infrastructure. The petrophysical measurements of extensive drill hole cores can improve deposit modeling and deep exploration.

The application of magnetic data to mineral exploration, petrophysics, petrology and geological interpretation is addressed in the literature [1–3]. Smith [4] provided a generic description of the geophysical characteristics of an iron oxide-copper-gold (IOCG) deposit. Furthermore, Sandrin and Elming [5] and Sandrin et al. [6] gave a more detailed description of the physical properties, petrology, and geophysics for IOCG. Recently, many petrophysical studies have been carried out to tackle the difficulties encountered in the modeling of magnetic data, such as remanence, demagnetization, and the effect of low magnetic latitudes. Austin et al. [7] used a constrained modeling of petrophysical data

on IOCG deposits in Australia. Clark [8] reviewed the magnetic effects of hydrothermal alteration on porphyry copper and IOCG systems. Fabris et al. [9] integrated geophysical, geochemical, and spectral methods to map the Punt Hill IOCG system. Sun and Li [10,11] inverted geophysical data with petrophysical constrains. Melo et al. [12] and Melo [13] applied physical property values to geophysical inversions to obtain a 3D geology characterization and differentiation of Cristalino iron oxide-copper-gold deposit in Carajás, Brazil. Costa et al. [14] used machine learning methods to predict a lithological map in the Carajás Cinzento lineament. Melo et al. [15] discussed the hidden potential of Carajás by exploring the geophysical characteristics of the Cristalino deposit. Recently, Martins et al. [16] applied geophysical and geological data to machine learning target generation in Carajás Mineral Province.

However, there is a lack of petrophysical studies that characterize the multiple hydrothermal alteration zones of IOCG mineralization to perform a 3D modeling. Moreover, there are few detailed studies that correlate statistical characteristics of magnetic susceptibility measurements with core samples and geology description.

At the Furnas Southeast deposit, which is the IOCG system studied in this research, multiple alterations are related to sigmoidal thrust shear zones that imprint variations of magnetic properties on the rocks within and surrounding the deposit. Structural stretching lineation controls the main ore shoots. Mineralization is represented by copper sulfides and gold, which is spatially and genetically associated with iron oxide. Copper-gold-disseminated mineralization was produced by biotite-garnet-grunerite-magnetite hydrothermal alterations with chalcopyrite and bornite high-grade ores, associated with the presence of magnetite.

Regardless, the complexity and spatial variability of hydrothermal alteration and mineralization makes it difficult to define a simple geological and geophysical exploration model. Therefore, due to different hydrothermal alterations and types impinging on mineralization and host rocks, a strong magnetization and magnetite content point toward one of the most important physical properties of the deposit as a possible tool for creating a geophysical exploration model—magnetic susceptibility.

To access data on the many geological entities that comprise the Furnas Southeast deposit, a careful procedure was designed that encompasses five broad phases. These phases state the agenda of the paper and the order in which it will be presented. The first phase is a brief review of IOCG deposits, description of the geological setting of Carajás, and hydrothermal alteration and mineralization assemblage of the studied deposit. The second phase is to devise a deposit magnetic anomaly and test the induced magnetization inversion. The third phase addresses extensive magnetic susceptibility measurements carried out on drill core samples from the deposit using a handheld magnetic susceptibility meter. The fourth phase is devoted to an extensive statistical analysis of these measurements. The aim is to characterize the magnetic susceptibility footprints for the prospect of copper-gold deposits, especially investigating the relationship between high-grade mineralization and magnetite content and distinguishing between the different magnetic susceptibility footprints of the hydrothermal alteration zones. The fifth phase sought to identify a careful geological matching of the findings and how they could help to understand the spatial distribution and behavior of geological entities in this deposit. A 3D model of these measurements separated the magnetic susceptibility spatial distribution associated with magnetite (Fe) hydrothermal alteration mineralization from the other various hydrothermal alteration types and host rocks.

As a conclusion, measurements and statistical analyses defined the magnetic susceptibility hydrothermal alteration footprints, followed by their careful space positioning in a 3D modeling. The aim was to produce the best possible spatial model depicting the variation of this physical property, and to define a susceptibility model for the local IOCG mineralization and its hydrothermal alterations.

Therefore, by having a set of prospective drill holes with a similar mineral association to the tested drill hole and its core samples, this approach is a simple and inexpensive way

to thoroughly understand the magnetic footprints of these geological entities using measurements, spatial positioning, and modeling. This can certainly improve the exploration of brownfield prospect/deposit minerals, as well as helping magnetic data inversion and modeling as prior information constrains in greenfield targets and magnetic geological drill cores description to deposit evaluation.

2. Geological Setting

2.1. Iron Oxide-Copper-Gold (IOCG) Deposits

All major IOCG deposits are rich in copper, gold and iron oxides and were originally defined as a unique type of deposit after the discovery and study of the Olympic Dam in the Gawler Craton, Southern Australia [17–19].

Williams et al. [20] present a discussion of possible IOCG origins based on the distribution of space related to time and geology. From an economic perspective, the most significant IOCG deposits are those in the coastal batholithic belt in Chile and Peru (Jurassic-Cretaceous extended continental margin arc); within the Gawler Craton and Cloncurry districts in Australia (late Paleoproterozoic to Mesoproterozoic, debated intracratonic or distal subduction-related settings); and in the Carajás province in Brazil (Archean, Amazon craton). Groves et al. [21] describe IOCG deposits from throughout Earth's history, the implications for origin and lithospheric setting, and the distinction from other epigenetic iron oxide deposits. Barton [22] addresses a comprehensive petrologic and geochemical characterization of iron oxide(-Cu-Au-REE-P-Ag-U-Co) systems. Logan et al. [23] discuss the relationship between IOCG and iron oxide-apatite (IOA) deposits with debatable deposit classification. A new IOCG categorization framework is proposed by Skirrow [24] based on tectonic and geological settings, mineralogy of oxide-sulfide occurrences, and ore geochemical properties.

Mougeot et al. [25] address the IOCG classification of the epigenetic copper deposits in the Carajás Province. Monteiro et al. [26] describe the spatial and temporal zoning of hydrothermal alteration and the mineralization in the Sossego IOCG deposit in Carajás Province. Xavier et al. [27] 2012 summarize the iron oxide-copper-gold systems of the Carajás Mineral Province. Campo-Rodrigues et al. [28] and Huang et al. [29] revealed new insights into Salobo and Alemão deposits in Carajás Province regarding magnetite and copper mineralization.

Recent hydrothermal alteration models for IOCG mineralization present characteristics, exploration vectors and alteration facies associated with iron oxide and alkali-calcic (IOAA) systems [30–32].

Due to the presence of iron oxides in the main types of IOCG deposits, an understanding of magnetic susceptibility behavior can improve the knowledge of this important mineralization. This study discusses the magnetic susceptibility response related to the geology of the Furnas Southeast deposit associated with magnetite. In the next section, we focus on regional geology, lithostratigraphy units and deposit geology.

2.2. Furnas Deposit Geological Setting

Carajás is known as an economically important metallogenic province where numerous types of mineral deposits have been found. In addition to IOCG mineralization, there are many types of deposits, such as banded iron formations, gold, manganese, mafic-ultramafic layered intrusions hosting platinum group elements, nickel laterite, and nickel sulfide deposits. In geotectonic terms, the Carajás Province is located within the Central Brazilian Shield at the southeastern portion of the Central Amazonian Province. The Transamazonian Province (Maroni-Itacaiúnas) borders it to the north and the Araguaia Belt borders it to the east [33].

The lithostratigraphy in the Carajás Mineral Province is complex. It consists mostly of Precambrian rocks that are overlain by younger sediments (Figure 1, [34,35]). The local lithostratigraphy is represented by several Precambrian units (Xingu, Pium and Luanga Complexes; Plaquê and Cateté Suites), Neoarchean metasedimentary and meta-volcano-

sedimentary sequences (Itacaiúnas Supergroup), Proterozoic anorogenic granitoids (granitic plutons with Lower/Middle Proterozoic ages), and Phanerozoic cover units [29,30].

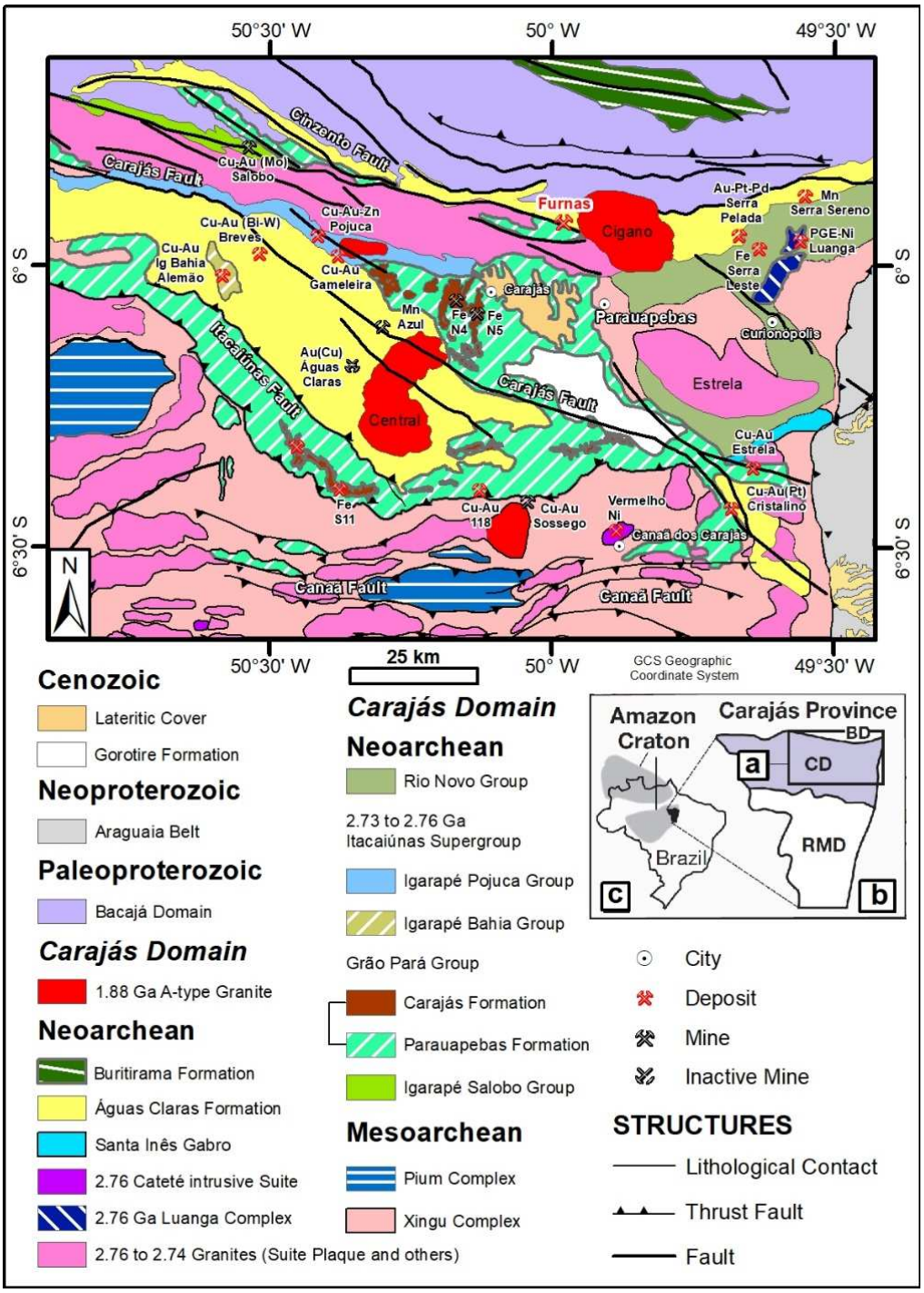

Figure 1. Geological map of the Carajás Mineral Province with the location of the Furnas deposit and the main Cu, Au, Fe, Mn, Ni, and Pt group element (PGE) deposits. (**a**) Location of the Carajás Geological Map in the regional setting. (**b**) Carajás Province map with the Carajás domain (CD) and Rio Maria domain (RMD). The Bacajá domain (BD) is located north of the Carajás domain. (**c**) Map of Brazil with the location of Carajás Province (in black) and the Amazon Craton (in gray) (Modified from DOCEGEO [35]; Araújo and Maia [36]; Barros and Barbey [37]; Vasquez et al. [38]; and Xavier et al. [27]).

The Furnas Southeast deposit is located along the west-northwest trending Cinzento transcurrent system, which is approximately 200 km long. The Cinzento lineament can be observed in the total magnetic intensity (TMI) map (Figure 2; magnetic data are discussed further). We can observe several anomalies along the Cinzento lineament that allow us to use a magnetic method and its physical property source as a mapping tool.

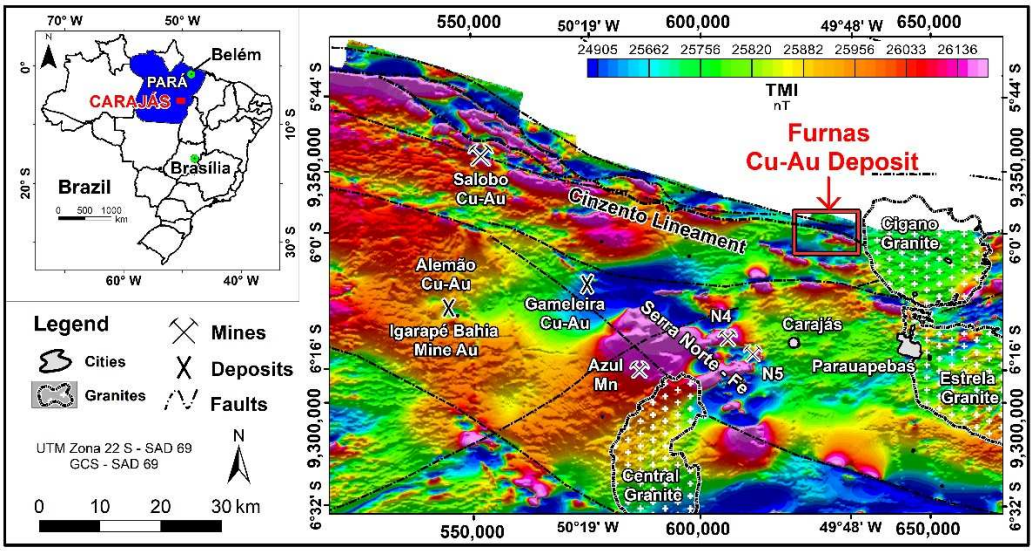

Figure 2. Total magnetic intensity of Carajás Mineral Province with the location of the Furnas deposit along the Cinzento lineament, mines, deposits, granites, and main faults.

The deposit is hosted in rocks correlated with the metamorphosed volcano-sedimentary types of the Grão Pará Group, which belongs to the Itacaiúnas Supergroup (2.76 Ga) and Águas Claras Formation (Wirth et al. [39]; Figures 1 and 3). Furnas deposit rocks can be correlated with supracrustal rocks from the Igarapé Salobo Group observed at the nearby Salobo Cu-Au deposit ([40,41]; light green areas in Figure 1). Interpretation of protolith rocks is difficult because of the intense metasomatic alterations that, in general, progress from high to low temperatures.

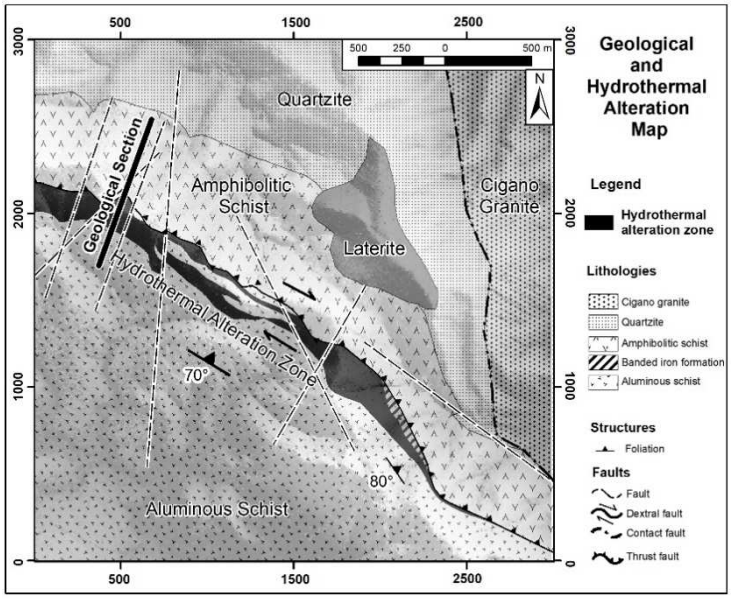

Figure 3. Geological and hydrothermal alteration zone map of the Furnas Southeast deposit; the location of the geological section shown in Figure 4 is indicated by the solid black line.

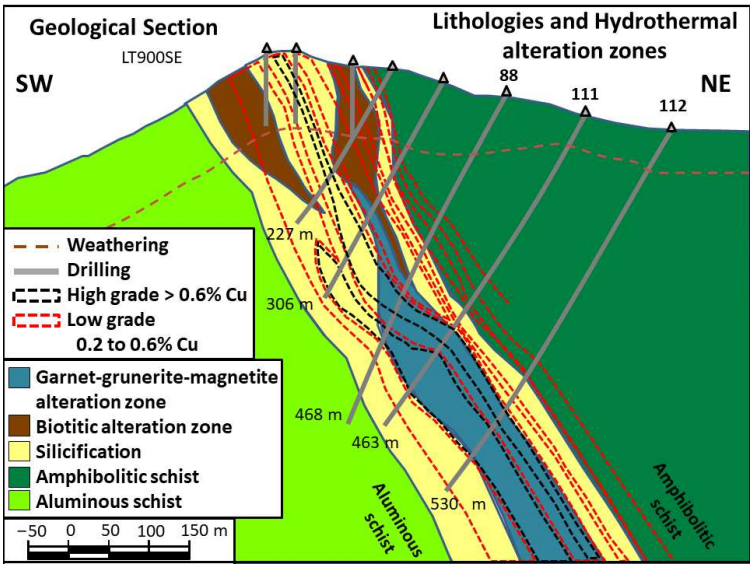

Figure 4. Geological section with the host rocks, hydrothermal alteration zones and mineralized zones. High-grade orebodies with values higher than 0.6% copper (modified from Vale S.A. [42]). Location of the section in Figure 3.

In the study area (3 km by 3 km), quartzites and schists host the deposit (Figure 3). The quartzites might be correlated with the Águas Claras Formation (yellow color in Figure 1). The aluminous schist contains andalusite-kyanite-sillimanite-staurolite and has been described as resulting from the deformation and metamorphism of aluminous pelitic sediments that are most likely correlated with the Águas Claras Formation. The amphibole schist is interpreted as the result of the deformation and metamorphism of volcanic rocks, most likely with protoliths being the Parauapebas Formation with the dashed light green legend in Figure 1. These are banded iron formations correlated to the Carajás Formation of Grão-Pará Group, as shown with dashed black lines in Figure 3 (dark brown color in Figure 1).

In the eastern portion, the anorogenic Cigano granite (Figure 3), aged 1.8 Ga [39], is described as an isotropic monzogranitic rock with portions of moderate primary foliation (red color in Figure 1). Cigano granite rocks are leucocratic with a gray-pinkish color, coarse-to-medium grain, and a monzogranitic composition with amphibole and biotite.

In the Furnas Southeast deposit, mineralization is situated along a shear zone that defines a contact between an amphibolitic schist (metavolcanic mylonitic rocks) to the north (hanging wall) and aluminous schist (metasedimentary mylonitic rocks) to the south (footwall; Figures 3 and 4). The Cinzento shear zone was intruded by the anorogenic Cigano granite (1.8 Ga A-type granite, red legend in Figure 1) to the east and continues northwestward towards the Salobo deposit ([39]; Figures 1 and 2). The region is metamorphosed from greenschist to amphibolite facies and has a deep lateritic weathering profile.

2.3. Hydrothermal Alteration and Mineralization

This section aims to describe the hydrothermal alteration and mineralization of Furnas Southeast Deposit. First, we present the approach used to reach the results. Second, a geological section that summarizes the alteration and mineralization shape is shown. Third, an overview of mineral assemblage and mineralization type is discussed. Finally, we detail the alteration zones.

Hydrothermal alteration characterizations were determined based on the drill cores macroscopic observations supported by petrographic studies and the presence of magnetite was first tested using a handheld magnet. Magnetic susceptibility measurements were subsequently acquired to show magnetic properties of the various lithologies and alteration zones and will be widely discussed in the next sections.

A cross section through the high-grade orebody with values higher than 0.6% copper displays the geology in the profile (Figure 4). The hydrothermal alteration zones have a lenticular shape and thicknesses of 20 to 600 m. The deposit is poorly exposed to a deep laterite profile about 60 m thick that reinforces the importance of using geophysical methods due to the lack of outcrops.

The copper-gold disseminated mineralization in the Furnas Southeast deposit has a biotite(K)-garnet(Ca)-amphibole(Na-Ca)-magnetite(Fe) hydrothermal alteration assemblage. While the hydrothermal alteration and mineralization type and intensity vary throughout the orebodies, a consistently strong alteration and mineralization paragenetic sequence can be identified.

A biotite-garnet-amphibole-magnetite hydrothermal assemblage shows a high-temperature alteration, whereas the subsequent low-temperature alteration shows a biotite-chlorite-tourmaline-carbonate-quartz-epidote-albite-hematite-magnetite assemblage. The high-grade mineralization itself is associated with magnetite-, chalcopyrite- (Figure 5a) and bornite-rich (Figure 5b) late-stage veins and breccias, paragenetically equivalent to the high-temperature assemblage. The hydrothermal alteration zones extension is approximately 9 km along the entire Furnas deposit. The study area is in the southeast portion of the deposit and is dominated by high-temperature alterations with the abundant presence of ferrimagnetic behavior due to large amounts of magnetite, which enable the use of magnetic susceptibility as an exploration tool.

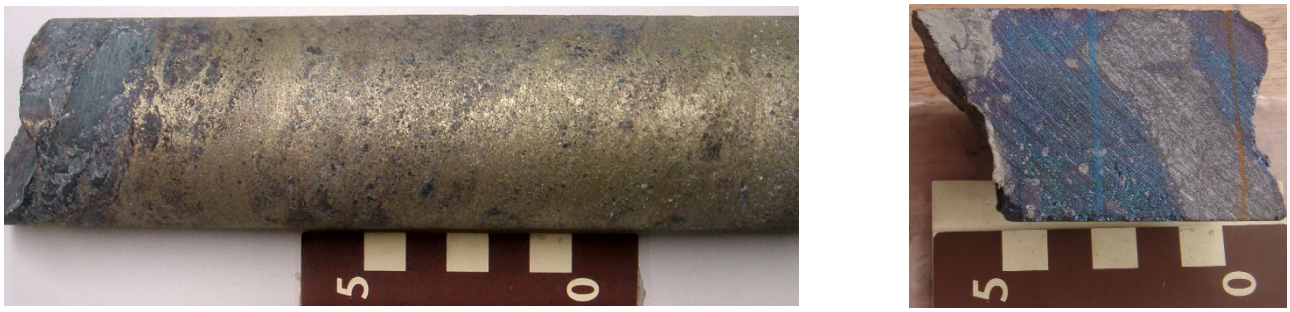

(**a**) (**b**)

Figure 5. Photographs of ore samples. Scale in centimeters. (**a**) Chalcopyrite and (**b**) bornite dominant veins and breccias with an amphibole-magnetite hydrothermal assemblage.

Sodic (Na), silicic (Si), potassic (K), calcic (Ca), sodic-calcic (Na-Ca) and massive magnetite (Fe) alterations host the mineralization with the dominant alteration minerals and textures described below.

Sodic (Na) alteration is the earliest alteration type of observed alteration. Sodic (Na) alteration is associated with albite veins in the Furnas Southeast deposit. However, this alteration is best observed in the Furnas Northwest deposit, outside of the study area, where host rocks consist of Furnas granite. With that, we do not investigate, in detail, this alteration type in this study.

A silicic alteration (Si) type is widely distributed over the deposit area that can completely transform the host rock. The silica saturation is uncommon in the Carajás IOCG Deposits and is likely related to intense hydrothermal alteration over deformed sedimentary rocks (quartzites) from Águas Claras Formation. The silica-rich alteration forms lenticular zones. Narrow bands of sericite and quartz characterize the silicic alteration (Si) type. The silicic alteration may also contain chalcopyrite and rarely bornite. Importantly, magnetite is absent. This type of alteration has a diamagnetic response.

The potassic (K) alteration type is common near the brittle-ductile and brittle deformed rocks. Mineralized bodies are commonly associated with potassic (K) zones that are essentially composed of biotite with a schistose texture and locally within tectonic-hydrothermal breccias cemented with biotite. In addition, the potassic (K) zone has a

significant association with garnet (Ca), magnetite (Fe) and silica (Si) alteration minerals. Despite the paramagnetic predominance, we expect ferrimagnetic responses due to the presence of magnetite.

The calcic (Ca) alteration type is concurrent with or subsequent to potassic (K) alteration. Calcic (Ca) alteration exhibits coarse-grained calcic garnet proximal to the mineralized zones with fine-grained calcic garnets found more distal. It typically overprints the potassic (K) alteration. The mineral assemblage includes calcic garnet-grunerite (Ca). The alteration occurs in association with bands of silicic alteration (Si). The garnet-grunerite calcic (Ca) alteration vary from isotropic to anisotropic textures, and from ductile to brittle-ductile deformations. This alteration can also occur in association with the presence of magnetite (Ca-Fe). We hypothesize that the calcic (Ca) alteration is predominantly paramagnetic due to garnet-grunerite responses, but it altered ferrimagnetic behavior in the magnetite assemblage (Ca-Fe). This alteration is associated with high Cu-Au grades.

The magnetite presence is directly associated with high-grade copper and gold mineralization. This stage of high iron metasomatism forms massive magnetite, and the Fe-rich fluid flow was structurally controlled. The magnetite alteration (Fe) type overprints the sodic-calcic (Na-Ca) alteration type and forms bands with the garnet-grunerite-magnetite assemblage (Ca-Fe). There is also a strong association with the brecciated silicification. We expected a strong ferrimagnetic response to the massive magnetite alteration (Fe).

The sodic-calcic (Na-Ca) alteration type is dominated by amphiboles (predominance of actinolite) and has variable amounts of quartz, tourmaline, and albite. We expect a paramagnetic behavior due to the dominance of silicates in this alteration zone. Chalcopyrite and bornite are found locally. This alteration type often occurs after the silicic (Si), potassic (K), and magnetite (Fe) alteration types. However, magnetite infiltrations appear with an expected ferrimagnetic response in the sodic-calcic (Na-Ca) alteration, which is dominated by the amphiboles (Na-Ca-Fe). In general, sulfidation occurs in association with these amphibole-magnetite assemblages (Na-Ca-Fe).

Subsequently, some final alteration types occur and are not discussed in detail in this study. The first is a new potassic (K) alteration process with biotitization that is followed by a strong chloritization (Chl) process, which partially or completely alters the rocks of the area, affecting local areas of hydrothermal breccias with mineralized chlorite-hematite-magnetite. The other late alterations are related to carbonation and silicification. Calcite occurs in association with quartz-hematite-magnetite-pyrite-chalcopyrite-epidote-albite-biotite-tourmaline veinlets.

The knowledge of minerals present in hydrothermal alteration zones is crucial for determining the correlation between the measured magnetic susceptibility and the diamagnetic, paramagnetic, and ferrimagnetic properties of the minerals. With that, the predominant mineralogical description in this section is key to the correct interpretation of mineralization magnetic susceptibility footprints.

3. Materials and Methods

As an indirect method, magnetometry is dependent on the source size, geometry, depth, latitude position, remanence, self-demagnetization, and anisotropy. To show the limitations of using indirect methods, we performed processing and inversion of airborne magnetic data. Magnetic data was acquired by a helicopter flown over the rugged terrain of the study area, and data collection finished in 2012. The acquisition used a sensor mounted on a boom. Draped survey flights were conducted at a nominal terrain clearance of 80 m above ground. The survey line spacing was 200 m, and the line direction was held at N 30° E. The ambient field has an inclination of −7.3°, a declination of −20.1°, and a field strength of 25,300 nT.

In this context of indirect methods limitation, the use of direct methods as magnetic susceptibility measurements can be more reliable. In this study, we performed almost eighteen thousand (17,789) magnetic susceptibility measurements along 17,739 m of drill cores from 69 drill holes (Figure 6). All the measurements were conducted on split drill

cores that were at least 40 mm thick to ensure a good contact area with the sensor. At least two measurements were performed at each point of the core samples to validate the value. We used the data measured with a susceptibility meter KT-10, with a sensitivity of 1×10^{-6} SI and range from -0.999×10^{-3} to 9999×10^{-3} SI, for statistical analyses and modeling. The data measured with susceptibility meter KT-9, with a sensitivity of 1×10^{-5} SI and range from 9.9×10^{-3} to 999.9×10^{-3} SI, were used separately and only for modeling.

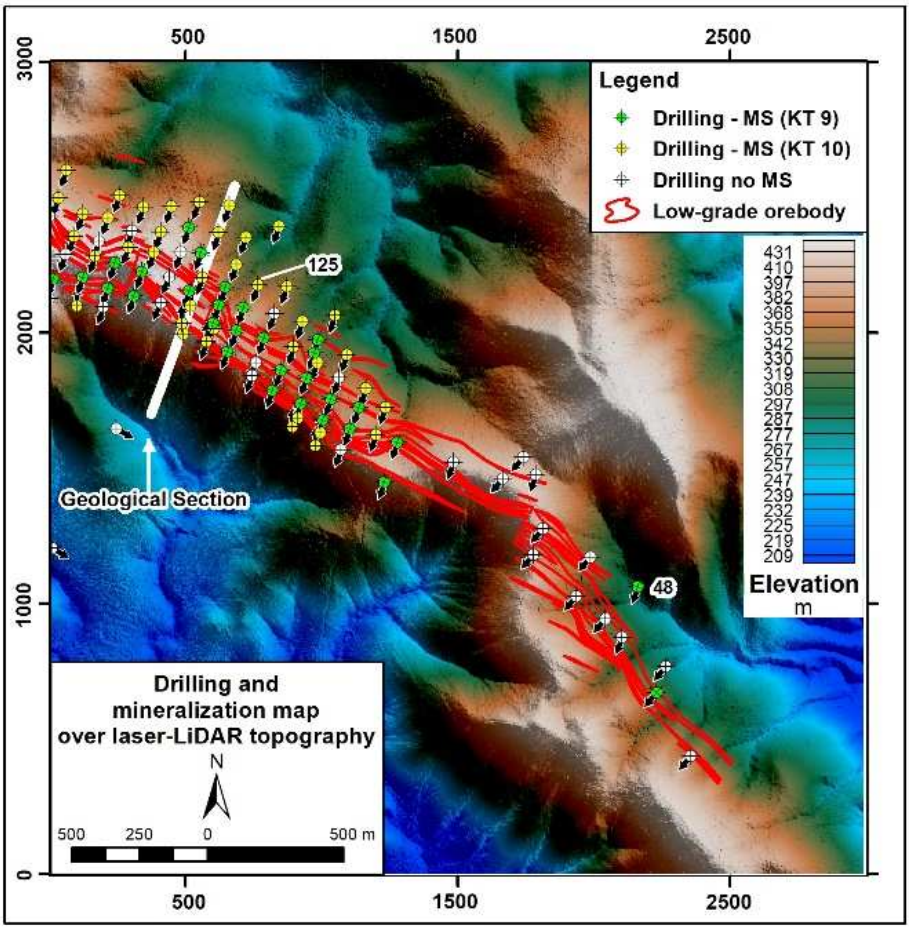

Figure 6. Drill hole location map. Measurement schematics: Lower sensitivity magnetic susceptibility (MS) measurements (KT-9) in green; higher sensitivity MS measurements (KT-10) in yellow; drill holes without MS measurements in white; and low-grade orebody projections at an elevation of 190 m in red. The geological section location (see Figure 4) is indicated in the map, and the numbers of drill holes, 48 and 125 used in this study, are indicated.

We established a quality-control procedure for all magnetic susceptibility measurements taken with hand-held instruments. We used statistical quality control to validate the duplicate measurements at each point; delete unmeaning and extreme values; evaluate outliers and wipe out noise and spikes. Due to the large variation between the sensitivities and the detection limits of the two susceptibility meters (KT9 and KT10), we separately analyzed and interpreted their specific databases. This was carried out because joined databases show means and histograms that do not represent the lithotypes and hydrothermal alteration zones.

Statistical analysis consisted of frequency diagrams of magnetic susceptibility values in uniform classes, and as such, characterized the susceptibility footprints for each lithotype and for each hydrothermal alteration zone. They indicated the susceptibility of data distribution and its populations, symmetries and dispersions.

The geochemical assays of iron, copper and gold from the drill cores were performed in the samples collected every 1 m. The analytical methods included a fire assay for gold (in g/t) and multi-acid/ICP-MS (inductively coupled plasma-mass spectrometry) for iron and copper (in percentage; Vale S.A. [42]).

In a flowchart of steps, Figure 7 summarizes the methods and materials used in this study.

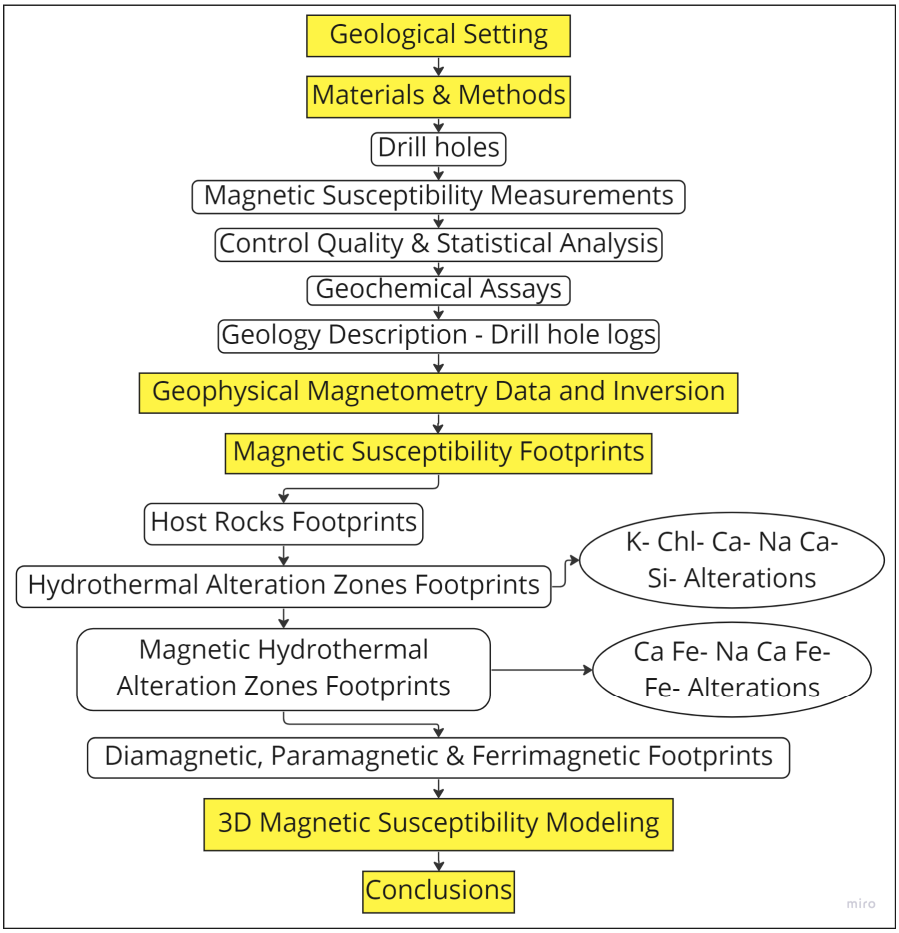

Figure 7. Flowchart that summarizes the steps, methods and materials used in this study.

4. Results

4.1. Geophysical Magnetometry Data

This section aims to describe the magnetic anomaly response and challenges in developing research at a low magnetic latitude with the presence of strong remanent magnetization. The magnetite is locally abundant in the hydrothermal alteration zone and has a strong magnetization that forms a high magnetic anomaly response in magnetic surveys. High-resolution airborne magnetic data were used to map the mineralization area and are discussed in this section.

4.1.1. Magnetic Anomaly

The TMI data show a high magnetic anomaly with a northwest-southeast direction (Figure 8a). The magnetic data delineate two main high-grade orebodies in the northwest and southeast portions of the study area (Figure 8b). The northwest high-grade orebody anomaly resembles a typical middle northern magnetic latitude anomaly: Positive values at its southern portion and large negative values at its northern portion. In contrast, the southeast orebody resembles the expected magnetic anomaly typical for magnetic equatorial regions, marked by negative values at its central portion and low positive values at

both the southern and northern portions (Figure 8a). The predominance of middle latitude behavior is related to strong remanent magnetization and self-demagnetization, as stated by Leão-Santos et al. [43]. In this study, we focused our research on the northwest anomaly.

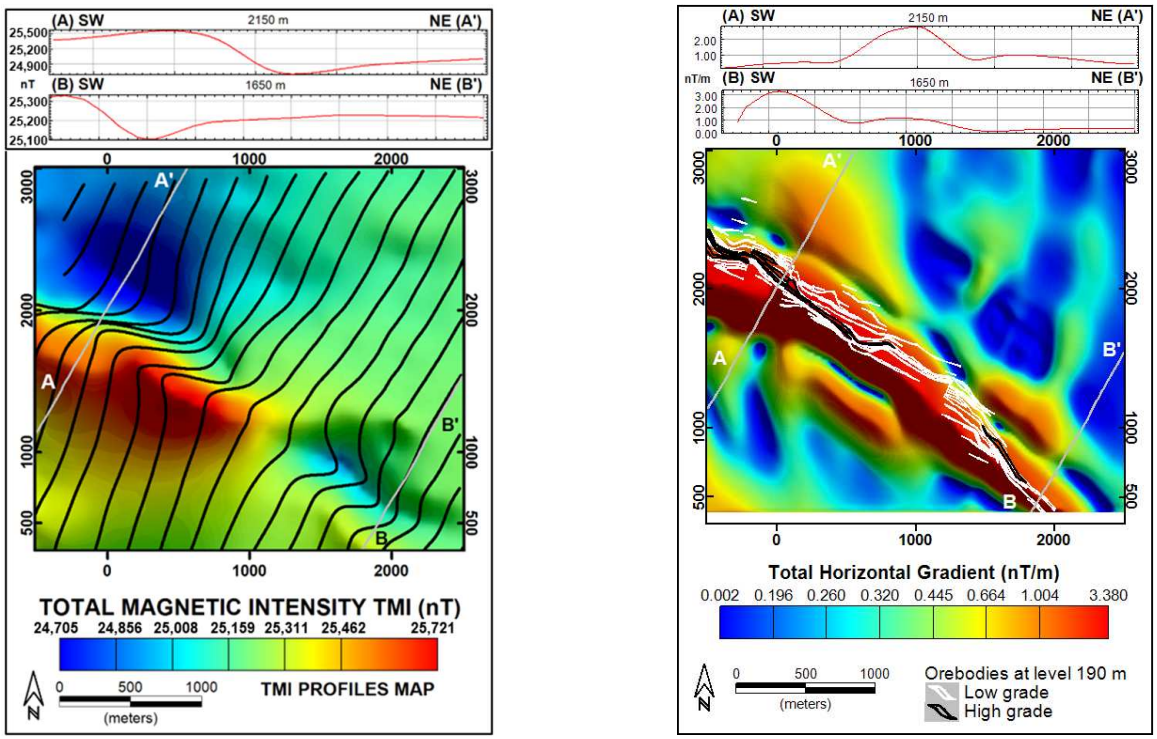

(**a**) (**b**)

Figure 8. (**a**) The observed total-field magnetic data of the Furnas Southeast deposit. Total magnetic intensity profiles are shown over each flight line in black traces. Units in nT. (**b**) Correlation of high-grade >0.6% copper (black lines) and low-grade between 0.2% and 0.6% copper (white lines) orebodies with a total horizontal gradient of the anomalous magnetic field. Units in nT/m.

The first- and second-order partial derivatives of TMI data in the X, Y, and Z directions can be combined in several ways for further magnetic data analysis. Modern methods for edge detection and depth to source estimation rely on horizontal and vertical derivatives. Total horizontal gradient shows the lateral limits of the anomaly sources and is one of the products that best delineates magnetic-related ore bodies (Figure 8b).

4.1.2. Induced Magnetization Inversion

In this study, we performed a 3D inversion of Furnas Southeast magnetic data with the algorithm presented by Li and Oldenburg [44] to assess the performance of the induced magnetization in the absence of site-specific geologic constraints, and thus understand the problems of this approach. This algorithm does not consider the challenge of magnetic response being displaced from source regions affected by strong remanent magnetization and self-demagnetization.

The method recovers a 3D distribution of the magnetic susceptibility. To perform the inversion, we used a mesh with cells of 25 m width in the x and y directions and thicknesses ranging from 12.5 m near the surface to 25 m in the vertical direction down to a depth of 780 m. To take into consideration any regional component that may be present in the data, padding cells were assembled to expand the mesh beyond the data area in all directions. We used 15,573 data stations to achieve a total of 261,919 cells in the final model.

The data inversion results were compared to the high magnetic susceptibility model in this study, which will be further explained (Figure 9). The results show a small coincidence

at the northwestern deep part of the area, a very low response at the center, and a non-coincident shifted response at the southwest part of the deposit. However, the results partially correlate with the known magnetic body. The lack and non-correspondence between the recovered 3D model of the effective susceptibility and the known magnetite-related body source (Figure 9) corroborate the discussed limitations of using induced magnetization 3D inverse physical property modeling for the Furnas Southeast Deposit.

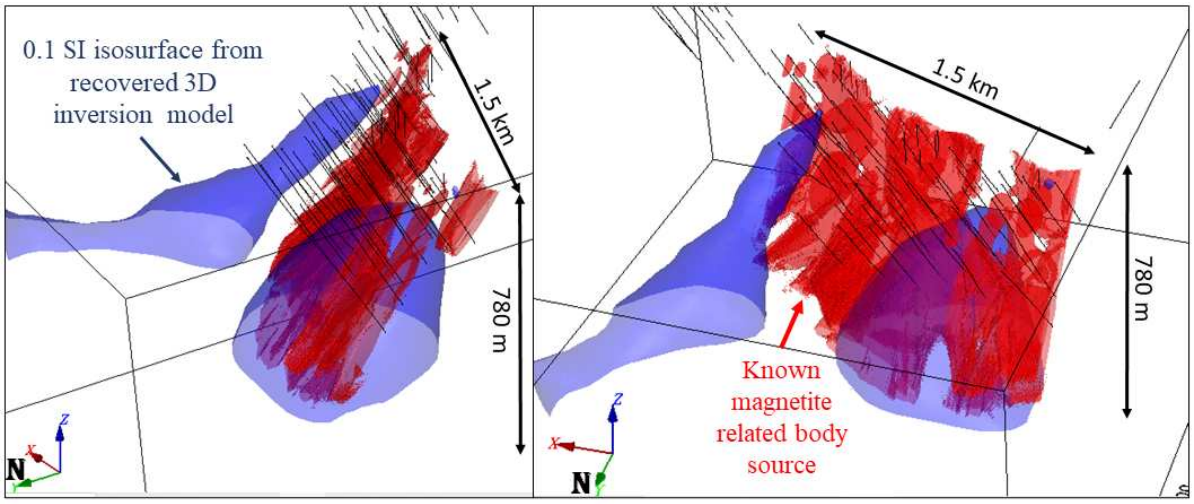

Figure 9. Correlation between the 0.1 SI isosurface from the recovered 3D-induced magnetization inversion model in blue and the known magnetite related body source from the high magnetic susceptibility model performed in this study that will be further explained in red. Drill holes in black traces. Views from northwest to southeast.

The significant remanence and self-demagnetization present in the Furnas deposit [38] and the resultant deviation of the magnetization direction severely limit the use of the common magnetic interpretation process and procedures that assume that the magnetization at the interpretation site has the same direction and sense as the current inducing field. Another incorrect assumption is that the magnetization is constant (at least in part) at the site. As such, magnetic data inversion techniques, even in localized and isolated magnetic anomalies, pose a great problem in terms of its real geological meaning (see discussions on the 3D inverse physical property modeling (susceptibility) for the local Furnas Southeast Deposit in Leão-Santos et al. [43]).

4.2. Hydrothermal Alteration Zones Magnetic Susceptibility

The hydrothermal alteration emplacing the orebodies is structurally controlled. Thus, the resulting deposit consists of several bodies of sigmoidal shape. The hydrothermal fluids pulse injections form magnetite (Fe) alteration zones by metasomatism with multiple magnetic source bodies that acquired remanent magnetization at different times and have different magnetization directions.

Magnetic susceptibility measurements were used to characterize the magnetic footprint of the Furnas Southeast IOCG deposit due to the lowest influence of remanent magnetization. Statistical analyses of the measured data are correlated to drill core lithotypes observations. Two drill holes (numbered 48 and 125) were selected to show characteristic magnetic susceptibility footprints because they best represent the lithotypes and their mineralization. Their individual core logs (Figures 10 and 11) were used to correlate magnetic susceptibility to the lithotypes and hydrothermal alteration zones.

Samples from the drill hole 125 show a strong correlation between lithotypes, alterations, and magnetic susceptibility (Figure 10). Magnetic zones (Fe) with high-grade mineralization are well-defined between a depth of 310 m and 380 m by their high magnetic susceptibility values (red box in Figure 10). This magnetic footprint is the main high-grade

mineralization zone in the deposit. Above this magnetite (Fe) zone, there is a zone with no magnetic susceptibility response between the depths of 205 m and 270 m, which correspond to silicic altered (Si) rocks with Cu and Au grades related to sulfide veins. This behavior can be observed in a depth range of 380 to 440 m in another mineralized silicification zone (Si) with Cu (Figure 10).

Similar behavior with no magnetic response in the silicic zone was also found in the data for drill hole 48 from the depths of 230 m to 400 m (Figure 11, big red box). Locally, this silicification zone hosts a very high grade (9% copper) vein-type mineralization, shown at a 240 m depth, and highlighted with a magenta arrow. Red arrows show non-magnetic hydrothermal alteration zones cutting host rocks. From the depths of 169 m to 211 m, the low magnetic susceptibility and high-grade iron footprints of the banded iron formation host rock are shown in small red boxes. The host rocks, amphibolitic schist (hanging wall) and aluminous schist (footwall) are shown in red bars (Figure 11).

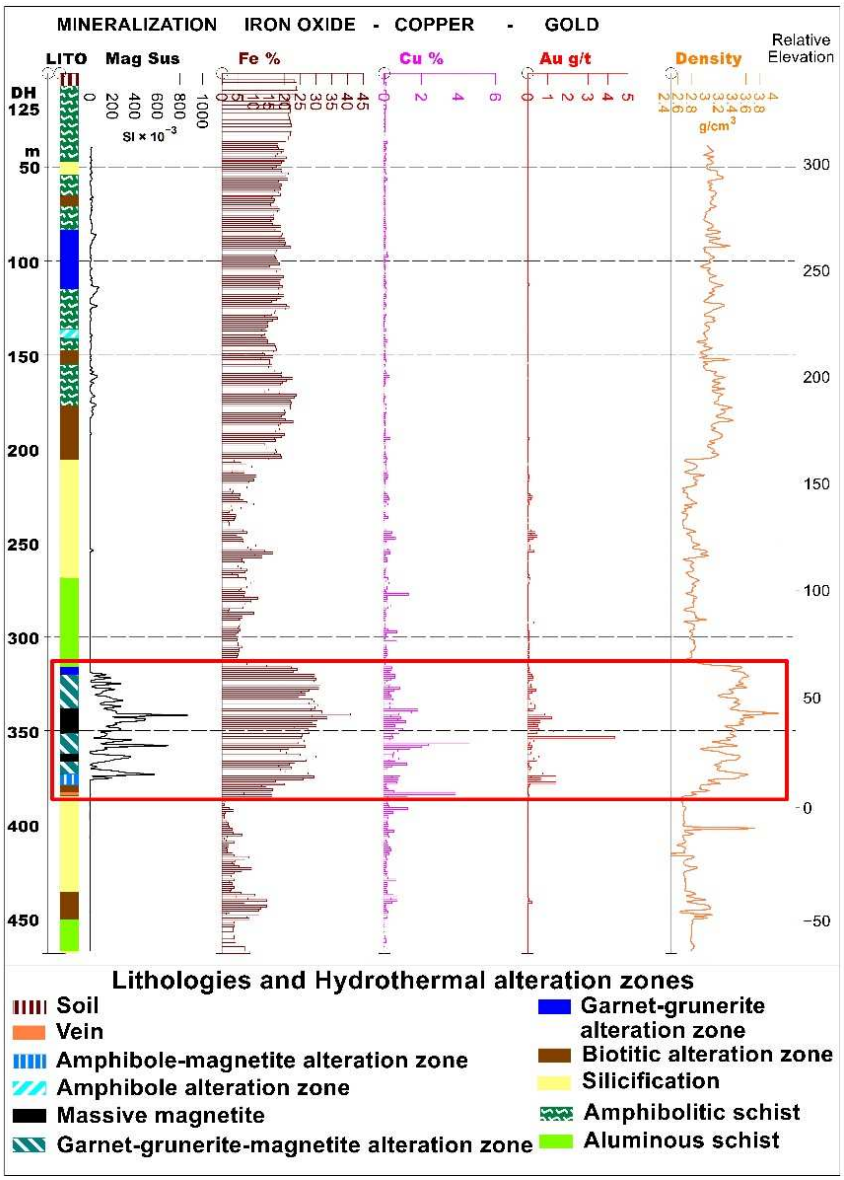

Figure 10. Sampling on the drill hole 125 log with the IOCG mineralization footprints: Hydrothermal alterations, magnetic susceptibility in SI $\times$ 10^{-3}, iron-grade geochemical assays in percentage, copper grade in percentage, gold in grams per ton, and density in grams per cubic centimeter. The red box shows the strong correlation between high-grade mineralization and high magnetic susceptibility.

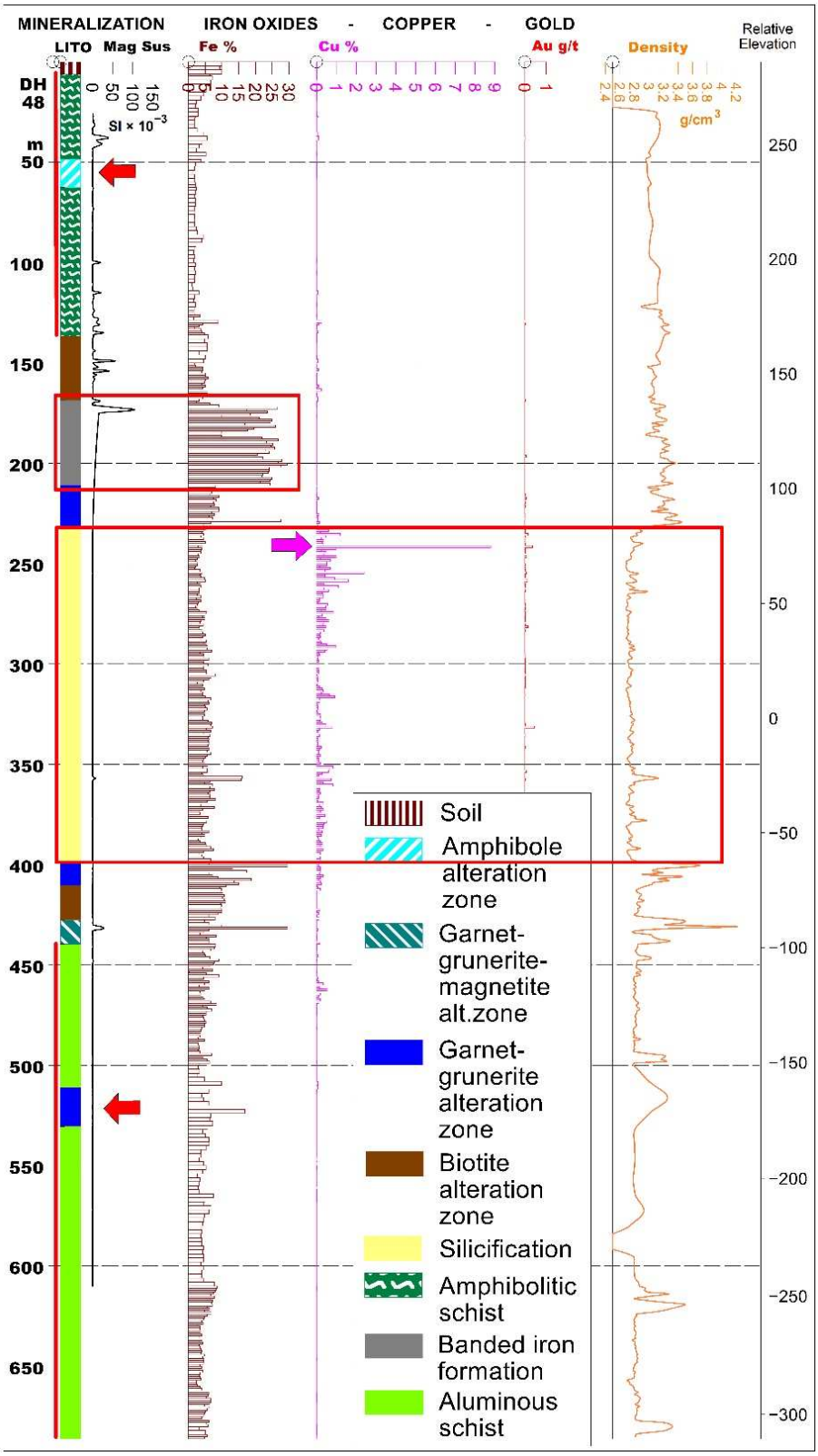

Figure 11. Sampling on the drill hole 48 log with the amphibolitic schist on top and an aluminous schist at the base (red bars) hosting the mineralized zone. Small red box: 169 m to 211 m depth, banded iron formation footprints with low magnetic susceptibility and high iron grade. Big red box: 230 m to 400 m depth, mineralized zone dominated by silicification. Red arrows: Non-magnetic hydrothermal alteration zones cutting host rocks. Magenta arrow: High-grade (9% copper) silicification vein type mineralization. No positive gold assay values were obtained below the legend.

The drill hole logs, as shown in Figures 10 and 11, were used to correlate the geology with the magnetic susceptibility statistical analyses, as described in this section. First, we briefly discuss host rocks and non-magnetic hydrothermal alteration zones, and finally focus on the main magnetic hydrothermal alteration zones. The understanding of the main mineralized magnetic susceptibility footprints can help magnetic investigations to achieve a successful exploration targeting.

4.2.1. Host Rocks

The magnetic susceptibilities medians of the main host rock lithotypes are aluminous schists (1.8×10^{-3} SI; Figure 12), amphibolitic schist (8×10^{-3} SI; Figure A1, Appendix A), banded iron formation (25×10^{-3} SI; Figure 13), monzogranite (0.8×10^{-3} SI; Figure A2, Appendix A), and quartzite (0.6×10^{-3} SI; Figure A3, Appendix A).

(**a**) (**b**)

Figure 12. Aluminous schist. (**a**) Statistics and histograms of the magnetic susceptibility measurements. (**b**) Core samples picture.

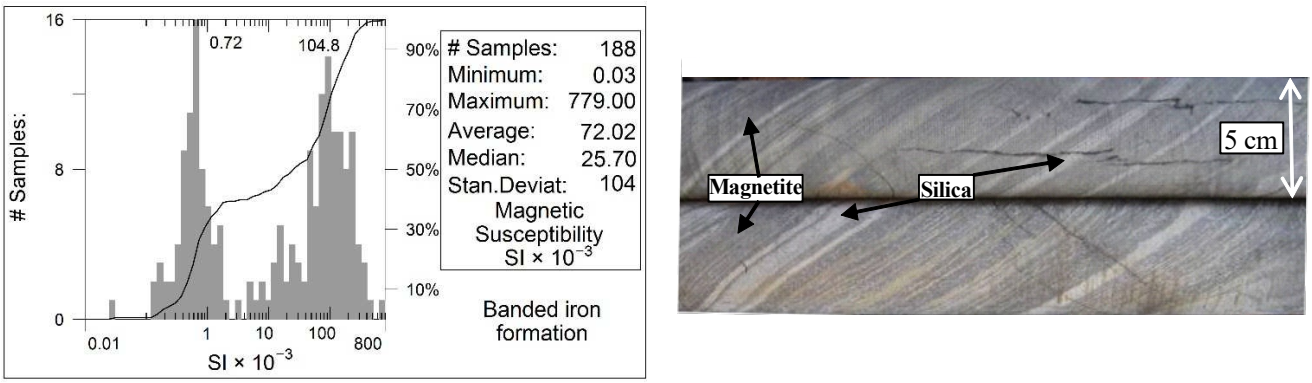

(**a**) (**b**)

Figure 13. Banded iron formation. (**a**) Statistics and histogram of the magnetic susceptibility measurements. (**b**) Core samples picture.

In the histogram of schist host rock susceptibilities, we can see that the distribution is a log normal distribution (Figures 12 and A1). The observed median value of 1.8 x 10^{-3} SI for the aluminous schists correlates well with the typical magnetic susceptibility values for schists, which are around 1.5×10^{-3} SI [45]. Drill hole 48 shows an amphibolitic schist at the top and aluminous schist at the base of the mineralized zone (Figure 11).

The banded iron formations mainly occur in the southeast portion of the studied area. Statistical analysis of the magnetic susceptibility measurements for these rocks presents a bimodal distribution with high values reflecting the ferrimagnetic behavior of the bands

with magnetite, which peaks at 104.8 × 10^{-3} SI, whereas the lower values reflect the diamagnetic behavior of the silica bands, which peak at 0.72 × 10^{-3} SI (Figure 13).

On drill hole 48, the non-mineralized banded iron formation footprint with predominant hematite and high iron geochemistry values can be observed between depths of 169 and 211 m (Figure 11 in small red box). A susceptibility response associated with the punctual presence of magnetite can be observed at the beginning of this interval (Figure 11).

4.2.2. Hydrothermal Alteration Zones Footprints

Garnet, amphibole, biotite, and chlorite are the main silicate alteration phases. These minerals have a paramagnetic behavior caused by the presence of Fe^{2+}, Fe^{3+} or Mn^{3+}. In general, the predominance of these paramagnetic minerals in the hydrothermal alteration zones, keeps the median susceptibility values between 4 × 10^{-3} SI and 7 × 10^{-3} SI, and the mean between 23 × 10^{-3} SI and 77 × 10^{-3} SI. The non-magnetic hydrothermal alterations are divided in five zones: Garnet-grunerite (Ca) with median 7.07 × 10^{-3} SI (Figure 14), amphibole (Na-Ca) with median 4.64 × 10^{-3} SI (Figure A4, Appendix A), potassic (K) with median 4.99 × 10^{-3} SI (Figure 15), chloritization (Chl) with median 5.23 × 10^{-3} SI (Figure A5, Appendix A), and silicification (Si) with median 0.60 × 10^{-3} SI (Figure 16).

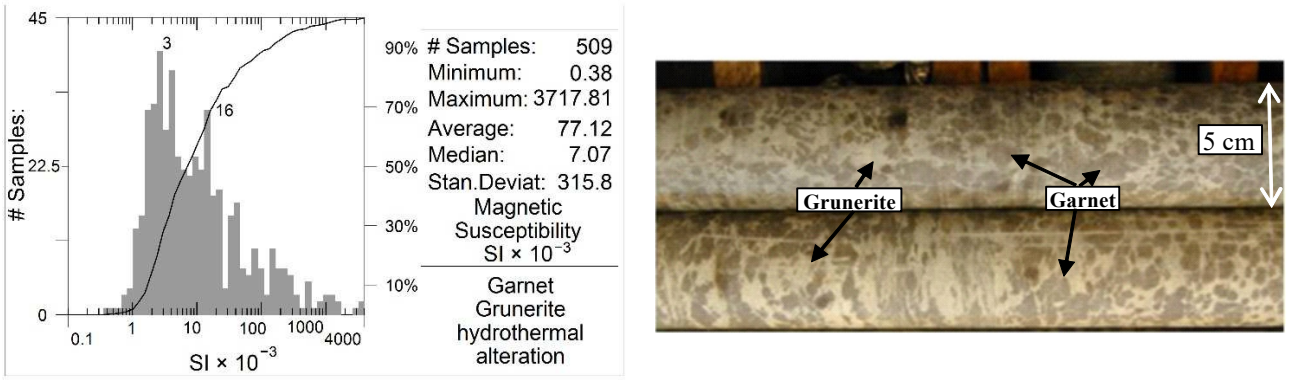

(**a**) (**b**)

Figure 14. Garnet-grunerite (Ca) hydrothermal alteration zone. (**a**) Statistics and histograms of the magnetic susceptibility measurements. (**b**) Core samples picture.

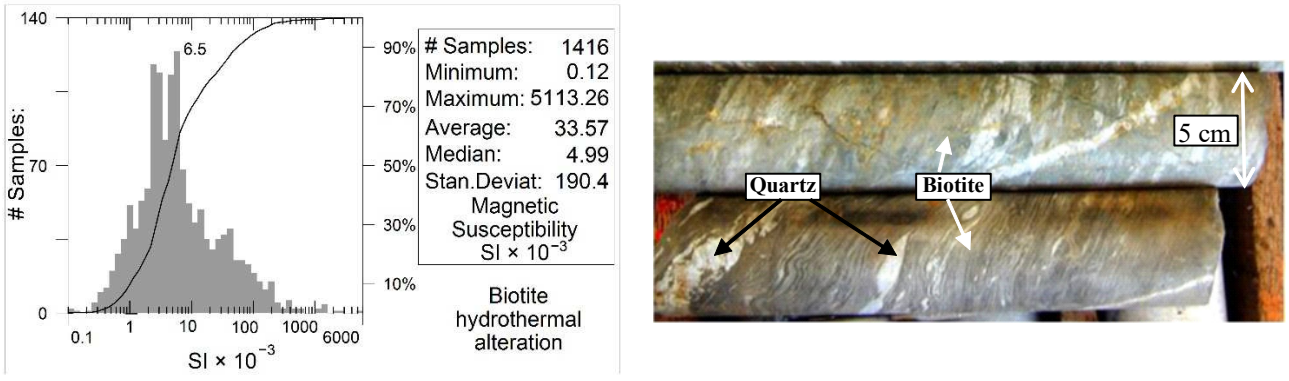

(**a**) (**b**)

Figure 15. Potassic (K) hydrothermal alteration zone. (**a**) Statistics and histograms of the magnetic susceptibility measurements. (**b**) Core samples picture.

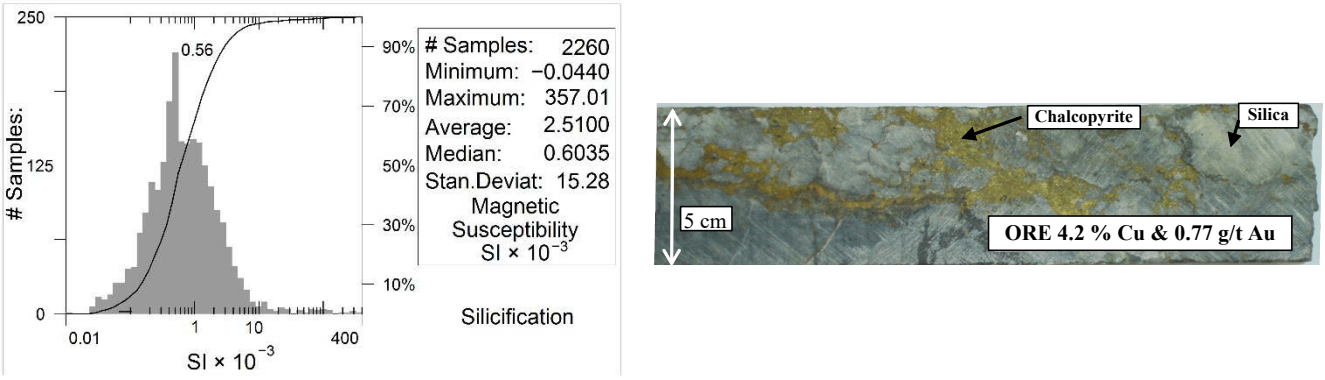

(**a**) (**b**)

Figure 16. Silicification zone. (**a**) Statistics and histogram of the magnetic susceptibility measurements. (**b**) Core sample picture.

However, within the hydrothermal alteration zones, we observe a trend of higher susceptibility values compared to host rocks, especially in the garnet-grunerite (Ca) and potassic (K) zones. Within these, the maximum values reach 3717 × 10^{-3} SI and 5113 × 10^{-3} SI, respectively, and likely reflect magnetite precipitated during the hydrothermal Ca-Fe- and K-Fe-typical alterations of IOAA systems (Figures 14 and 15). The only exception is the silicic alteration. Some silicates can appear as ferrimagnetic because of impurities such as magnetite. In complex hydrothermal environments, these impurities become common. These minerals start to show remanence and exhibit hysteresis. Biotite can be both paramagnetic (if non-altered) or ferrimagnetic (if altered). In addition, magnetite commonly occurs between the biotite and chlorite sheets planar voids (Figures 15 and A5, Appendix A), as well as in fractures associated with this type of alteration. Together, these phenomena account for the higher observed susceptibilities within the altered rocks.

The garnet-grunerite (Ca) and amphibole (Na-Ca) hydrothermal alteration zones have a close relationship with the low-to-medium grade mineralized zones. This can be seen in drill hole 125, between the depths from 83 m to 115 m (garnet-grunerite Ca), 137 m to 142 m (amphibole Na-Ca), and 316 m to 320 m (garnet-grunerite Ca) (Figure 10). This can also be seen in drill hole 48, between the depths from 211 m to 231 m and 400 m to 411 m (garnet-grunerite Ca) (Figure 11). The magnetic footprint of the mineralized garnet-grunerite (Ca) and amphibole (Na-Ca) hydrothermal alteration zones show low susceptibility values. In drill hole 48, between the depths from 49 m to 63 m and 510 m to 530 m (Figure 11, highlighted by red arrows), we can observe non-magnetic amphibole and garnet-grunerite (Ca) hydrothermal alteration zones cutting host rocks, respectively (Figure 11).

The potassic (K) and chloritization (Chl) hydrothermal alteration zones' footprints are the presence of a biotite and chlorite, respectively, which may or may not be associated with mineralization. In drill hole 125 (Figure 10), we can see that the depths from 70 m to 75 m the potassic (K) zone have no mineralization, and the depths from 435 m to 449 m have medium-high-grade mineralization.

The only magnetic susceptibility behavior exception in the hydrothermal alteration zones is the silicification (Si) type. The silicification is an overprint, unrelated to the main stage of magnetite (Fe)-related Cu-Au mineralization. This uncommon Carajás IOCG behavior is likely associated with quartzite host rocks hydrothermally altered in shear zones. Since quartz is diamagnetic, it is expected to have negative values, as observed, with a minimum of -0.04×10^{-3} SI. The histogram for the silicic alteration type shows a typical log normal distribution with a median value of 0.6×10^{-3} SI, a mean value of 2.51×10^{-3} SI and a maximum value of 357×10^{-3} SI (Figure 16).

The presence of paramagnetic minerals and instrumental limitations to measure negative values justifies the low positive susceptibility values. In the drill cores, an abundance of

silicification is closely related to the low- to high-grade mineralization (Figures 10 and 11). However, in many places, it can also be associated with extremely high-grade mineralization with up to a 9% copper content (Figure 11 highlights a 241 m depth with a magenta arrow) due to the presence of veins and breccias (see the picture in Figure 16).

4.2.3. Magnetic Hydrothermal Alteration Zones Footprints

Massive magnetite (Fe), garnet-grunerite-magnetite (Ca-Fe) and amphibole-magnetite (Na-Ca-Fe) hydrothermal alteration zones.

Magnetite is the most abundant ferrimagnetic mineral in the hydrothermal alteration zones and has high susceptibility values. The median magnetic susceptibility values decrease from the massive magnetite (Fe) alteration zone with 855 $\times$ 10^{-3} SI (Figure 17ab) to the garnet-grunerite-magnetite (Ca-Fe) alteration zone with 395 $\times$ 10^{-3} SI (Figure 17cd) and the amphibole-magnetite (Na-Ca-Fe) alteration zone with 269 $\times$ 10^{-3} SI (Figure 17ef). Among the magnetite-rich (Fe) alteration zones, the mean susceptibility values are 1896 $\times$ 10^{-3} for the massive magnetite (Fe) zone (Figure 17a), 1446 $\times$ 10^{-3} for the amphibole-magnetite (Na-Ca-Fe) zone (Figure 17e), and 1280 $\times$ 10^{-3} for the garnet-grunerite-magnetite (Ca-Fe) zone (Figure 17c). Both the median and mean are consistent with the observations for the drill core samples, which shows that the massive magnetite (Fe) hydrothermal alteration zone has a higher magnetite content than the garnet-grunerite-magnetite (Ca-Fe) and amphibole-magnetite (Na-Ca-Fe) zones (Figure 10).

In the massive magnetite (Fe) alteration zone histogram, there is a susceptibility population centered at high values around 800 $\times$ 10^{-3} SI, which is near the median of 855 $\times$ 10^{-3} SI and represents the predominance of magnetite (Figure 17a).

In the garnet-grunerite-magnetite (Ca-Fe) alteration zone histogram, the distribution becomes more complex. It shows two populations of susceptibility values. The highest valued population represents the massive magnetite footprint. The lower-value population has a significant concentration of paramagnetic minerals, such as grunerite and garnet (Figure 17c).

The amphibole-magnetite (Na-Ca-Fe) alteration zone histogram indicates that the values are very widely distributed, which is a result of the greater amphibole type mineral presence and high values associated with magnetite presence (Figure 17e).

This variation from high to intermediate and low values was observed in the drill cores, where the garnet-grunerite (Ca) and amphibole (Na-Ca) alteration zones are constantly altered by the inputs of magnetite, producing a great fluctuation in the susceptibility measurements (Figure 10).

The garnet-grunerite-magnetite (Ca-Fe) alteration occurs with a greater abundance relative to the amphibole-magnetite (Na-Ca-Fe) alteration zones. In addition, the garnet-grunerite-magnetite (Ca-Fe) alteration has higher a correlation with the massive magnetite (Fe) zone (Figure 10).

Descriptively, differentiating banded iron formation from the magnetite (Fe) hydrothermal alteration zone along the drill core observations becomes more difficult when magnetite and silicic banding is present. However, when comparing the susceptibility values, this difference is easily noticeable. Between the depths from 310 m to 380 m in drill hole 125 (Figure 10), the magnetite (Fe) hydrothermal alteration zone is marked by a high increase in the values of magnetic susceptibility, iron, copper, gold and density, when compared to the banded iron formation in drill hole 48 between the depths from 169 m to 211 m (Figure 11). Banded iron formations are not mineralized and normally show low values for susceptibility, iron content and density when compared to the magnetite (Fe) hydrothermal alteration zone. This difference can be observed when looking at the median values, which is 182 $\times$ 10^{-3} SI for the banded iron formation (Figure 13) and 855 $\times$ 10^{-3} SI for the massive magnetite (Fe) hydrothermal alteration zone (Figure 17a). The median value of the banded iron formation is low, even when compared to the medians of the garnet-grunerite-magnetite (Ca-Fe) (395 $\times$ 10^{-3} SI; Figure 17c) and amphibole-magnetite (Na-Ca-Fe) (269 $\times$ 10^{-3} SI; Figure 17e) hydrothermal alteration zones.

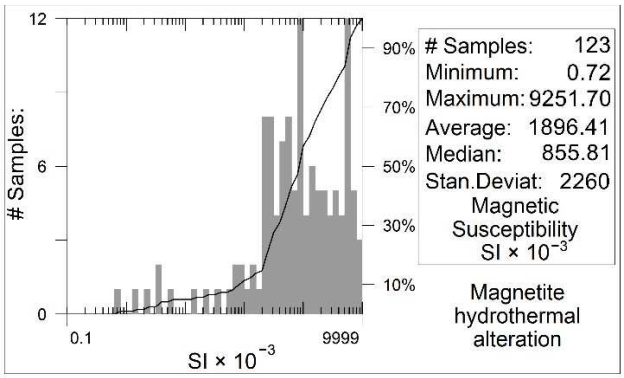

(**a**)

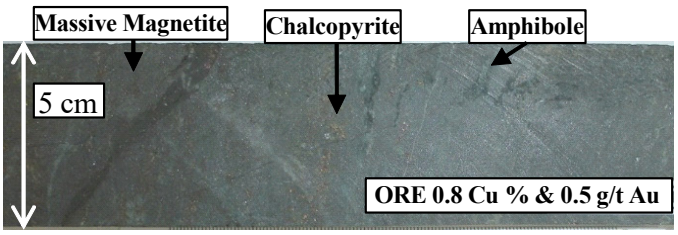

(**b**)

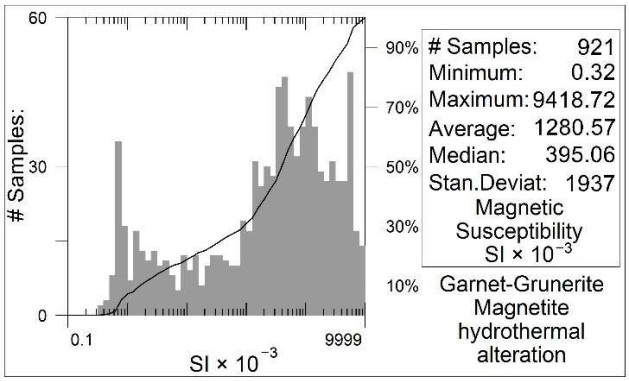

(**c**)

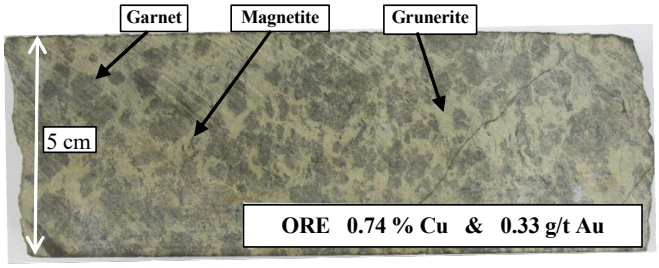

(**d**)

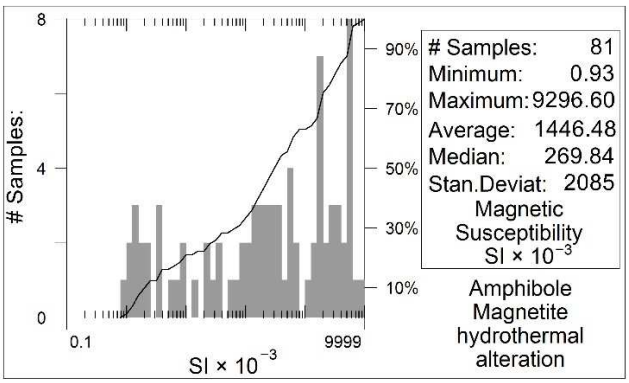

(**e**)

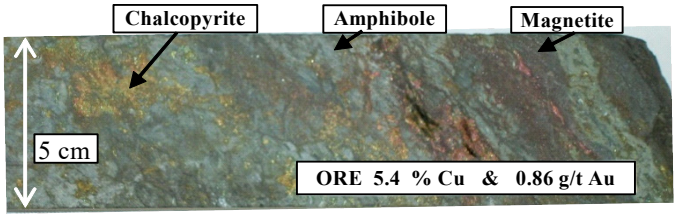

(**f**)

Figure 17. (**a**,**c**,**e**) Statistics and histograms of magnetic susceptibility measurements for magnetite rich-alteration types. (**b**,**d**,**f**) Core samples pictures of magnetite rich-alteration types. (**a**,**b**) Massive magnetite (Fe) hydrothermal alteration zone. (**c**,**d**) Garnet-grunerite-magnetite (Ca-Fe) hydrothermal alteration zone. (**e**,**f**) Amphibole-magnetite (Na-Ca-Fe) hydrothermal alteration zone.

4.2.4. Multiple Hydrothermal Alteration Zones Magnetic Susceptibility Footprints

Table 1 summarizes the magnetic susceptibility values correlated with lithotypes and their mineralogy. High median values (between 25 and 855 $\times$ 10^{-3} SI) address lithotypes bearing ferrimagnetic minerals; in this case, magnetite. The highest values are associated with massive magnetite (Fe) in the hydrothermal alteration zones (855 $\times$ 10^{-3} SI). We observe additional high values in the garnet-grunerite-magnetite (Ca-Fe)- and amphibole-magnetite (Na-Ca-Fe)-altered rocks (395 and 269 $\times$ 10^{-3} SI, respectively). High values are observed in some unaltered rocks, such as the banded iron formations (25 $\times$ 10^{-3} SI).

The intermediate median values (between 1.8 and 8.8 $\times$ 10^{-3} SI) are representative of the garnet-grunerite (Ca), amphibole (Na-Ca), chlorite (Chl) and biotite (K) hydrothermal alteration zones, likely due to the more paramagnetic presence of minerals, as opposed to ferrimagnetic magnetite. In addition, the amphibolitic and aluminous schist lithotypes (host rocks) also have intermediate values. The lowest median values (between 0.6 and 0.8 $\times$ 10^{-3} SI), negative in minimum values (-0.04×10^{-3} SI), are correlated with granite and quartzite lithotypes, as well as the silicic alteration type. This was interpreted to be caused by paramagnetic and diamagnetic minerals abundance (Table 1).

Table 1. Magnetic susceptibility (SI $\times$ 10^{-3}) statistics associated with mineralogy, lithotypes and hydrothermal alteration zones. The predominant associated minerals are in the same color of magnetic mineral classes and their representative magnetic susceptibility values. Med: Median, Min: Minimum, Max: Maximum.

	Lithotypes	Alteration Type	Mineralogy (Petrography)	Med	Min	Max
Ferrimagnetic	Massive magnetite hydrothermal alteration	Magnetite (Fe)	Magnetite ± amphibole (grunerite, actinolite, hornblende = hastingsite) ± quartz	855	0.72	9251
	Garnet-grunerite-magnetite hydrothermal alteration	Calcic-magnetite (Ca-Fe)	Garnet (almandine), amphibole (grunerite), magnetite ± biotite ± chlorite	395	0.32	9418
	Amphibole-magnetite hydrothermal alteration	Sodic-calcic-magnetite (Na-Ca-Fe)	Amphibole (actinolite), magnetite ± garnet ± quartz ± biotite ± chlorite	269	0.93	9296
	Banded iron formation	Host rock	Magnetite, silica	25.7	0.03	779
Paramagnetic	Garnet-grunerite hydrothermal alteration	Calcic (Ca)	Garnet (almandine), amphibole (grunerite) ± quartz ± chlorite ± biotite	7	0.38	3717
	Amphibole hydrothermal alteration	Sodic-calcic (Na-Ca)	Amphibole (actinolite) ± quartz ± biotite ± chlorite	4.64	0.51	1618
	Chlorite alteration	Chloritization (Chl)	Chlorite	5.23	0.61	1488
	Biotite hydrothermal alteration	Potassic (K)	Biotite, quartz, plagioclase, phengite ± garnet	4.9	0.12	5113
	Amphibolitic schist	Host rock	Amphibole (grunerite), quartz ± hornblende = hastingsite	8.84	0.27	4026
	Aluminous schist	Host rock	Quartz, biotite, sericite, andalusite, staurolite, silimanite ± garnet ± chlorite	1.8	−0.003	155
Diamagnetic	Monzogranite	Host rock	Quartz, plagioclase, microcline, biotite, chlorite (±pegmatites, granophyres)	0.83	0.19	99
	Quartzite	Host rock	Quartz ± sericite	0.6	−0.03	2.9
	Silicification	Silicic (Si)	Silica, sericite	0.6	−0.04	357

4.3. Magnetic Susceptibility Footprints Interpretation

The complexity of IOCG deposits in the Carajás region poses a challenge to establishing a geophysics exploration model due to the structural control, multiple hydrothermal alteration zones, ore texture, depth of formation, remanence, demagnetization, and low magnetic latitude.

The existence of extensive drill cores from the geological evaluation program encouraged attempts to find another model for this IOCG deposit based exclusively on direct magnetic susceptibility measurements and their footprints.

As such, we designed a thorough process as an alternative approach to obtaining a geological 3D physical property model for the Furnas Southeast Deposit. First, we performed extensive measurements, and an efficient method was established. Second, the statistical analyses presented above provided all the foundations for a spatial characterization of the deposit based solely on this property statistical footprint.

With the understanding of mineral predominant content that is associated with magnetic susceptibility measurements, we compared all lithotypes and hydrothermal alteration zones with magnetic susceptibility in a box plot to define the three main ferrimagnetic, paramagnetic, and diamagnetic footprints. A synthesis shows the magnetic susceptibility behavior of the various rocks and alteration types (Figure 18).

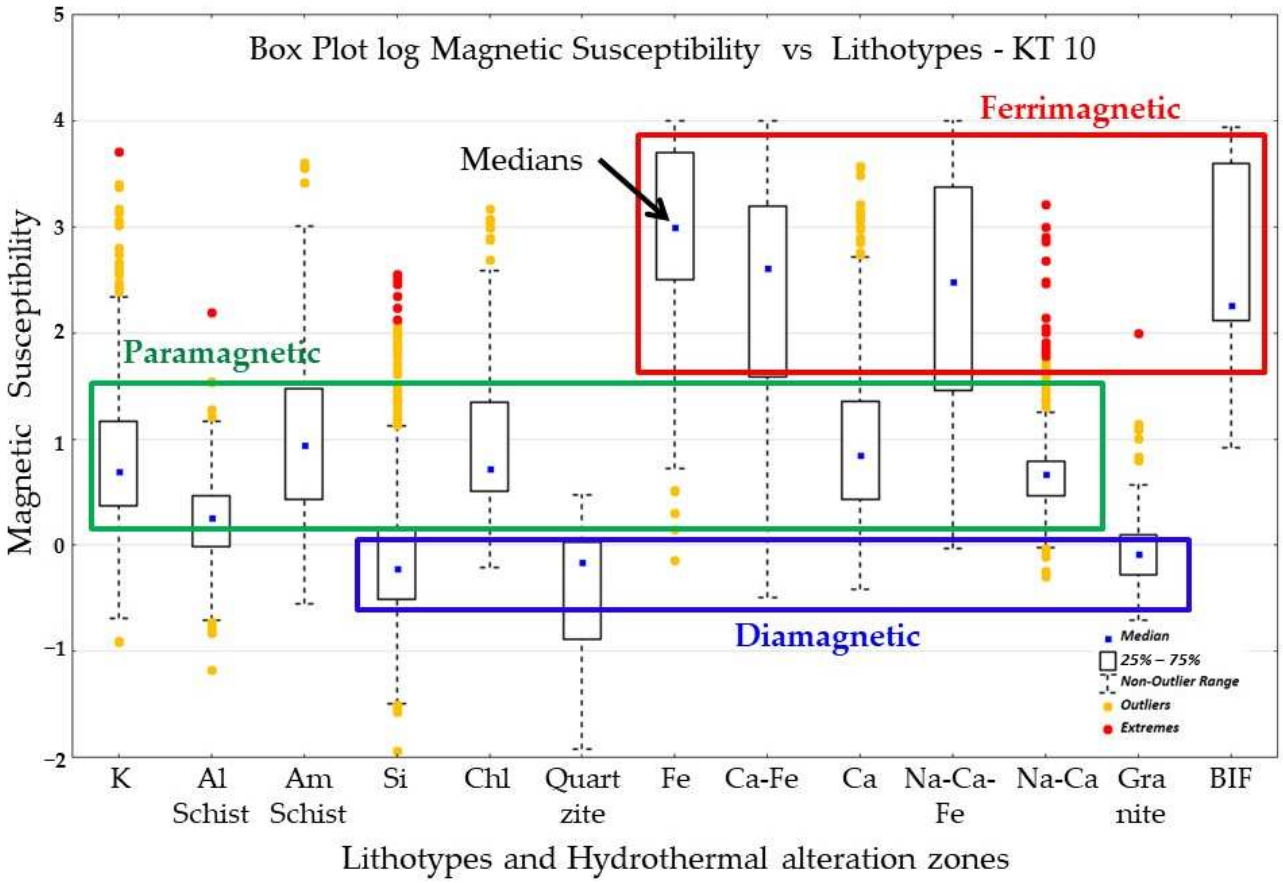

Figure 18. Box plot log of magnetic susceptibility (SI) versus lithotypes with values from the higher sensitivity susceptibility meter (KT-10). The ferrimagnetic, paramagnetic, and diamagnetic minerals dominances is represented in red, green, and blue rectangles, respectively. K = potassic, Al = aluminous, Am = amphibolitic, Si = silicification, Chl = chloritization, Fe = ferric, Ca = calcic, Na = sodic, BIF = banded iron formation.

The study of the range of the three main ferrimagnetic, paramagnetic, and diamagnetic footprints, together with the spatial position of the measurements on drill holes, is important for the next phase of the research that is the three-dimensional modeling of the deposit.

4.4. Magnetic Susceptibility 3D Modeling

The careful positioning in space of the determinations gathered was able to produce the best possible spatial model for this physical property of the local IOCG mineralization and their hydrothermal alterations. Its spatial distribution and behavior can help to understand the geological entities for this local mineralization.

We divided the georeferenced measurements subspace into 5 m cubic cells and interpolated using a 3D kriging algorithm [46]. The deposit strike direction is N 60° W (300° Azimuth). The transverse direction is where most of the used samples are gathered. To address these different sample density directions, a weighting function was used to normalize this effect.

To define the best cut-off, we calculated the average of the ferrimagnetic hydrothermal alterations medians with a final value of 506×10^{-3} SI (855 + 395 + 269 = 1519/3 = 506). Using this, we defined the physical 3D model, including host rocks and hydrothermal alteration zones with predominant diamagnetic and paramagnetic minerals footprints values lower than 500×10^{-3} SI from the high-sensitivity equipment (KT-10) and values lower than 60×10^{-3} SI for those measured with the low-sensitivity equipment (KT-9) (Figure 19). In the magnetic susceptibility 3D model, including hydrothermal alteration

zones with predominant ferrimagnetic mineral footprints, the values are greater than 500×10^{-3} SI from the high-sensitivity equipment (KT-10) and greater than 60×10^{-3} SI for those measured with the low-sensitivity equipment (KT-9) (Figure 19). These values were selected from the statistical analyses, as previously mentioned. The two envelope surfaces of different equipment bound susceptibilities values higher than the threshold values for both cases. They complement each other because of the different distributions of the drill holes used in the measurements (Figure 6). It is important to emphasize that the susceptibility model reflects only the northwestern portion of the study area, which is where the studied drill holes are located (Figure 6).

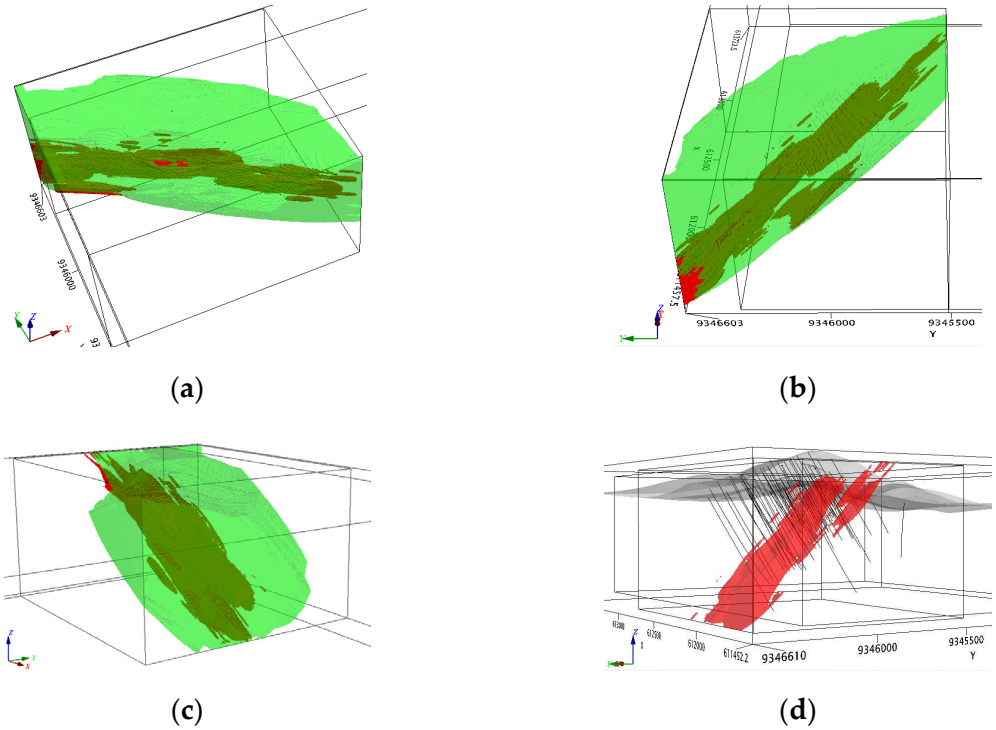

(**a**) (**b**)

(**c**) (**d**)

Figure 19. The 3D magnetic susceptibility models interpolated using a 3D kriging algorithm [46]. The red model includes hydrothermal alteration zones with predominant ferrimagnetic minerals footprints values greater than 500×10^{-3} SI from the high-sensitivity equipment (KT-10) and values greater than 60×10^{-3} SI for those measured with the low-sensitivity equipment (KT-9). The green model includes host rocks and hydrothermal alteration zones with predominant diamagnetic and paramagnetic minerals footprints with values lower than that cited above. The 3D kriging with 5 m cubic cells. Drill holes in black traces and topography in the gray surface. (**a**) Top view from SW to NE. (**b**) View from E to W. (**c**) View from SE to NW. (**d**) View from NW to SE.

This susceptibility model versus ore concentration, when seen in detail, shows the direct correlation between the magnetite (Fe) hydrothermal alteration zones, represented by high magnetic susceptibility values (envelope of the values greater than 500×10^{-3} SI) (Figure 20a), and high-grade orebodies with values higher than 0.6% copper (Figure 20b). However, the Si alteration is represented by low magnetic susceptibility values and wraps the magnetic Fe alteration. The continuation of interpolation in depth can suggest the main interpreted trend of ore (Figure 20a). A dip difference can be observed between the sections, also on the right (Figure 20b) of the mineralized zones that crop out at the hill crest, whereas in the model (Figure 20a), the magnetic zone projects the surface downslope to the SW. These differences can be explained due to the absence of measurements on the weathered lateritic profile and interpolation algorithm trend.

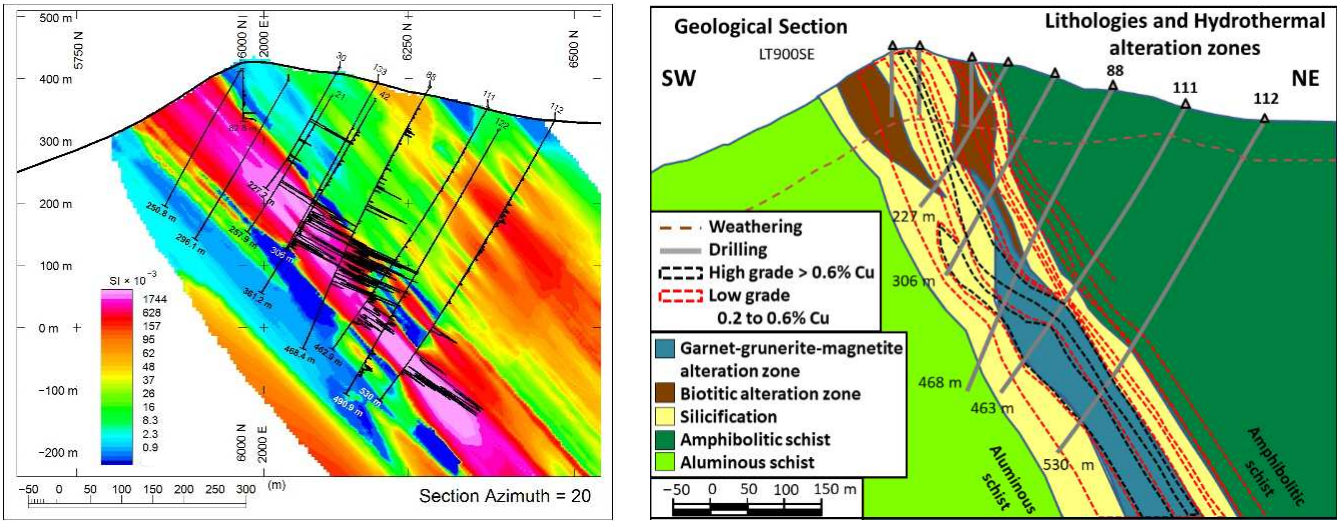

(**a**) (**b**)

Figure 20. Good correlation between (**a**) magnetic susceptibility model represented with magnetic susceptibility measured on drill cores (black line profiles along drill hole lines). (**b**) High-grade orebodies with values higher than 0.6% copper (dashed black lines) represented in the geological section with the host rocks, hydrothermal alteration zones and mineralized zones (Modified from Vale S.A. [42]). The location of sections is shown in Figures 3 and 6.

The 3D magnetic susceptibility model's strike and dip shows a good fit with the ore-grade 3D model from extensive drilling. Comparison of the susceptibility model with low-grade (0.2 to 0.6% Cu; Figure 21a) and the high-grade (threshold limit >0.6% Cu; Figure 21b) ore model from 69 drill holes (Vale S.A. [42]) shows this excellent correlation.

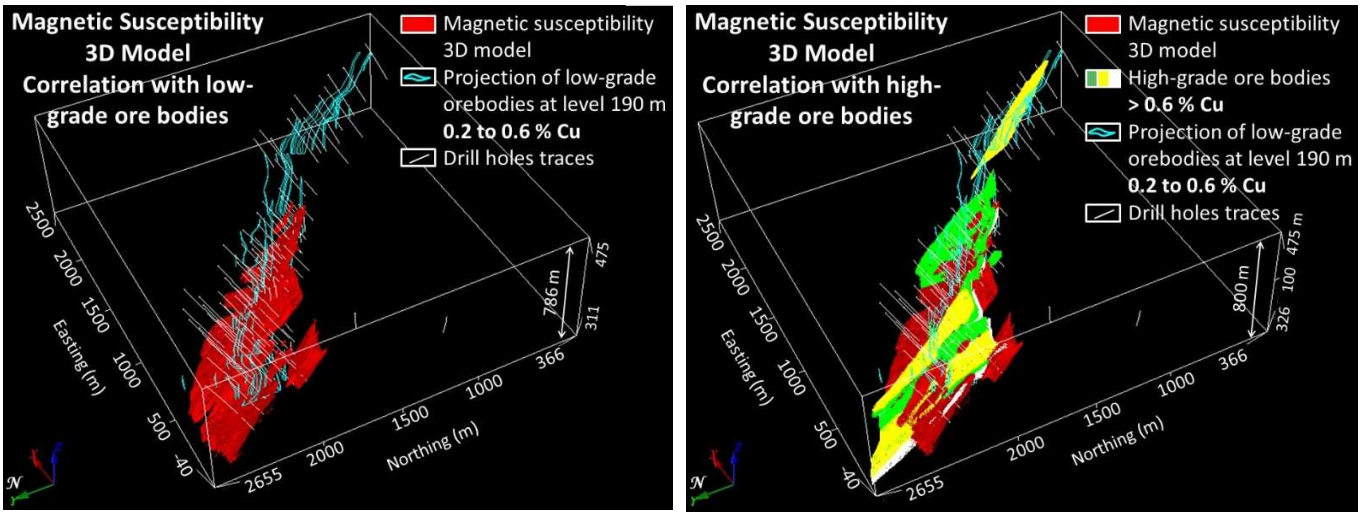

(**a**) (**b**)

Figure 21. (**a**) Correlation of the three-dimensional magnetic susceptibility model with the projection of low-grade copper orebodies (0.2 to 0.6% Cu) at the level 190 m. (**b**) Correlation of the three-dimensional magnetic susceptibility model with the high-grade copper orebodies (ore threshold limit higher than 0.6% Cu) from extensive drilling. The isosurface cutoff of the 3D magnetic susceptibility model with predominant ferrimagnetic mineral footprints show values greater than 500×10^{-3} SI for the high-sensitivity equipment (KT-10) and values greater than 60×10^{-3} SI for those measured with the low-sensitivity equipment (KT-9).

It is interesting to note that the efficient quality control of measured data discussed herein is crucial for the correct analysis of measured magnetic susceptibilities and interpolation of a reliable 3D model, as thoroughly discussed in this paper.

5. Conclusions

The comprehensive petrophysical characterization and geological-geophysical interpretations presented in this study are useful for: (i) Characterizing magnetic susceptibility footprints of ore zones and hydrothermal alteration zones, as long as the magnetite plays an important role in the mineralization formation and constitution process; (ii) quantitative assistance in the correlation and geological interpretation of mineralized lithotypes; (iii) quantitative support in sections interpretation for the generation of geological and ore models; (iv) improving and validating the use of magnetic surveys as well as mineral prospecting techniques and geophysical equipment; (v) providing for the constrained inversion of magnetic data, excellent prior information applied to grassroots and greenfield exploration programs; and (iv) appropriate use of extensive drill cores available in new brownfield explorations.

In the Furnas Southeast deposit, the massive magnetite (Fe), garnet-grunerite-magnetite (Ca-Fe) and amphibole-magnetite (Na-Ca-Fe) hydrothermal alteration zones are the most important due to their direct relationship with chalcopyrite and bornite sulfides (mineralization high-grade with values higher than 0.6% copper). The statistical analyses indicate a strong contrast between magnetic and non-magnetic hydrothermal alteration zones. The obtained results enable predominant diamagnetic (median 0.0006 to 0.00083 SI) and paramagnetic (median 0.0018 to 0.0088 SI) footprints to be separated from ferrimagnetic (median 0.269 to 0.855 SI) footprints to construct a 3D model with their distributions, which traces the well-known boundaries of the studied mineralization. This study approach is a very important and non-expensive method to support IOCG deposits brownfield and greenfield exploration programs.

Author Contributions: Conceptualization, M.L.-S., R.M. and Y.L.; methodology, M.L.-S., R.M., Y.L. and M.I.R.; validation, M.L.-S. and R.M.; formal analysis, M.L.-S. and R.M.; investigation, M.L.-S., R.M., Y.L., and M.I.R.; resources, M.L.-S., M.I.R. and B.Z.; data curation, M.L.-S.; writing—original draft preparation, M.L.-S., R.M. and Y.L.; writing—review and editing, M.L.-S., R.M., Y.L., M.I.R. and B.Z.; visualization, M.L.-S.; supervision, M.L.-S., R.M., Y.L. and M.I.R.; project administration, M.L.-S.; funding acquisition, M.L.-S. All authors have read and agreed to the published version of the manuscript.

Funding: This research was funded by Vale S.A. Company, Educational Short-Term Assignment, 18 March 2011. This study was financed in part by the Coordenação de Aperfeiçoamento de Pessoal de Nível Superior—Brasil (CAPES)—Finance Code PDEE 1058/11-8.

Data Availability Statement: Data are available within the article.

Acknowledgments: The authors would like to thank Vale S.A. Company for their support and permission to use geophysical and geological data in this research project. We thank Joaquim Feijó for the extensive measurements, as well as geophysicist Cantidiano Freitas and geologists Otávio Rosendo and Arthur Cardoso for valuable geological discussions. We also would like to thank Misac Nabighian (*in memoriam*) who advised us in some aspects of data processing.

Conflicts of Interest: The authors declare no conflict of interest.

Appendix A

In this appendix, we complement this study with the statistics, histograms, and description of host rocks and hydrothermal alteration zones not presented in the paper.

Appendix A.1 Host Rocks

Amphibolitic schists were found to have higher susceptibility values in comparison to aluminous schist. The median was of 8.8×10^{-3} SI and the mean value of 36×10^{-3} SI (Figure A1). The large number of samples in these schists (3119) reflects the large extension

drilled in the amphibolitic schist to intercept the mineralized targets (2085 samples), which is the cap host rock.

The monzogranite rocks are affected by albite hydrothermal alteration. These rocks have low-magnetic-susceptibility values, which likely reflect the predominance of paramagnetic minerals in the rock, such as feldspar, plagioclase, and biotite, and diamagnetic minerals such as quartz. The median value is 0.83×10^{-3} SI, and the mean value is 3.5×10^{-3} SI, (Figure A2). The small number of samples (61) is a result of the low occurrence of these rocks in the Furnas Southeast deposit.

The quartzite shows low magnetic susceptibility values. For quartzite, the minimum value of -0.039×10^{-3} SI (Figure A3), is due to the diamagnetic characteristics of the quartz, which include weak susceptibility and negative values in its purest form. The statistical analysis of quartzite samples shows a low median value and mean of 0.66×10^{-3} SI (Figure A3). These values are high for pure quartzite. However, negative values probably do not occur in abundance due the elevated presence of paramagnetic minerals, such as sericite, and equipment limitations.

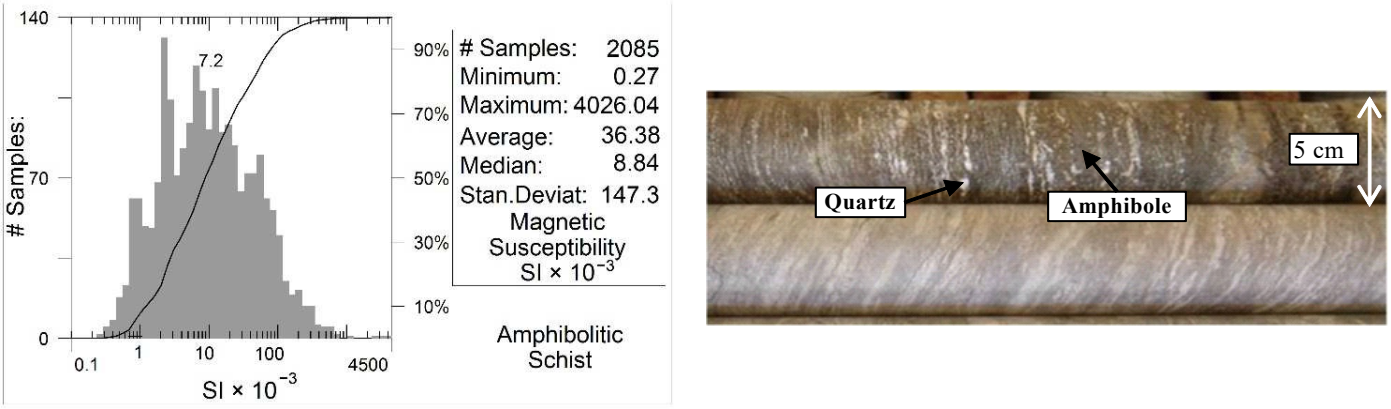

Figure A1. Amphibolitic schist. (**a**) Statistics and histograms of the magnetic susceptibility measurements. (**b**) Core samples picture.

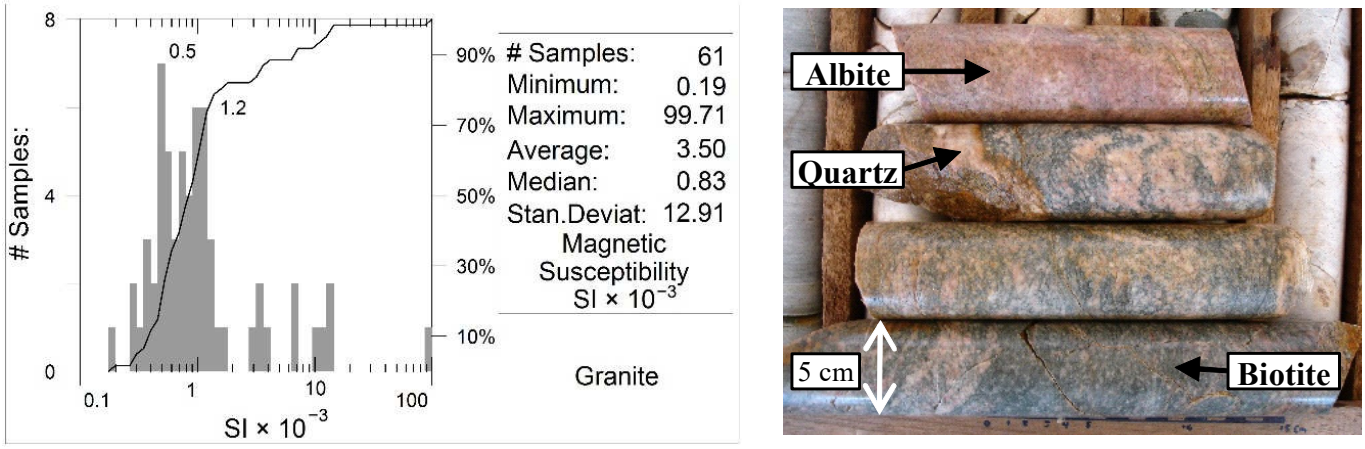

Figure A2. Granite. (**a**) Statistics and histograms of the magnetic susceptibility measurements. (**b**) Core samples picture.

(**a**) (**b**)

Figure A3. Quartzite. (**a**) Statistics and histograms of the magnetic susceptibility measurements. (**b**) Core samples picture.

Appendix A.2 Hydrothermal Alteration Zones

The amphibole (Na-Ca) hydrothermal alteration zone has a median of 4.64 × 10^{-3} SI and an average of 23 × 10^{-3} SI (Figure A4). The picture in Figure A4 shows a chalcopyrite mineralized sample with 1.4% of copper grade.

The chlorite (Chl) hydrothermal alteration zone may or may not be associated with mineralization. This alteration has low susceptibility values, with a median of 5 × 10^{-3} SI (Figure A5). The variation from low and intermediate values is interpreted to be the result of magnetite precipitation along fractures or between sheets of chlorite (Chl-Fe). The hydrothermal process of chloritization (Chl) is strong. It partially or completely alters the rocks of the area.

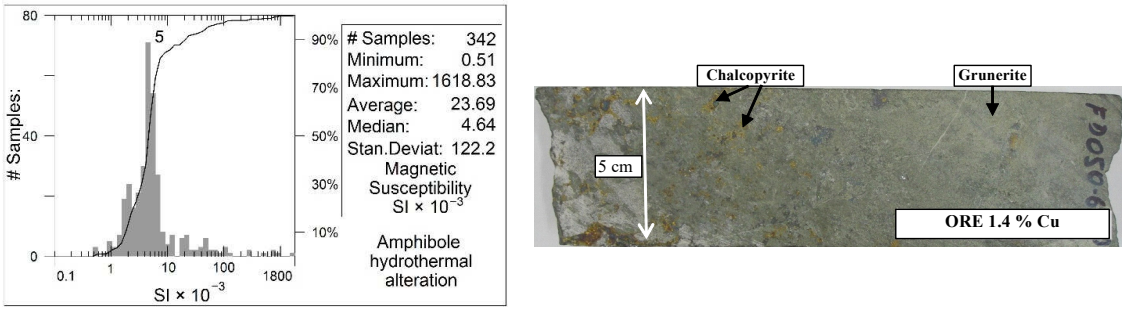

(**a**) (**b**)

Figure A4. Amphibole (Na-Ca) hydrothermal alteration zone. (**a**) Statistics and histograms of the magnetic susceptibility measurements. (**b**) Core sample picture.

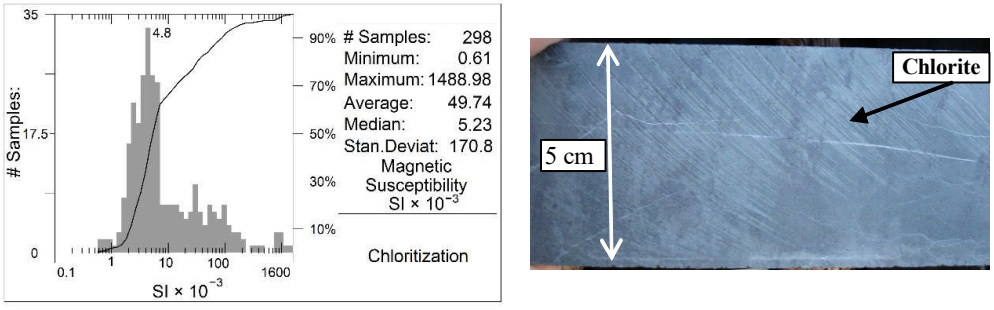

(**a**) (**b**)

Figure A5. Chloritization (Chl). (**a**) Statistics and histograms of the magnetic susceptibility measurements. (**b**) Core sample picture.

References

1. Clark, D.A.; French, D.H.; Lackie, M.A.; Schmidt, P.W. Magnetic petrology: Application of integrated rock magnetic and petrological techniques to geological interpretation of magnetic surveys. *Explor. Geophys.* **1992**, *23*, 65–68. [CrossRef]
2. Clark, D.A. Magnetic petrophysics and magnetic petrology: Aids to geological interpretation of magnetic surveys. *J. Aust. Geol. Geophys.* **1997**, *17*, 83–103. Available online: http://hdl.handle.net/102.100.100/224915?index=1 (accessed on 15 June 2021).
3. Clark, D.A. Magnetic petrology of igneous intrusions: Implications for exploration and magnetic interpretation. *Explor. Geophys.* **1999**, *30*, 5–26. [CrossRef]
4. Smith, R.J. Geophysics of iron oxide-copper-gold deposits. In *Hydrothermal Iron Oxide-Copper-Gold and Related Deposits: A Global Perspective*; Porter, T.M., Ed.; PGC Publishing: Adelaide, Australia, 2002; Volume 2, pp. 357–367.
5. Sandrin, A.; Elming, S. Physical properties of rocks from borehole TJ71305 and geophysical outline of the Tjårrojåkka Cu-prospect, northern Sweden. *Ore Geol. Rev.* **2007**, *30*, 56–73. [CrossRef]
6. Sandrin, A.; Edfelt, Å.; Waight, T.E.; Berggren, R.; Elming, S. Physical properties and petrologic description of rock samples from an IOCG mineralized area in the northern Fennoscandian Shield, Sweden. *J. Geochem. Explor.* **2009**, *103*, 80–96. [CrossRef]
7. Austin, J.R.; Schmidt, P.W.; Foss, C.A. Magnetic modeling of iron oxide copper-gold mineralization constrained by 3D multiscale integration of petrophysical and geochemical data. Cloncurry District, Australia. *Interpretation* **2013**, *1*, T63–T84. [CrossRef]
8. Clark, D.A. Magnetic effects of hydrothermal alteration in porphyry copper and iron-oxide copper-gold systems: A review. *Tectonophysics* **2014**, *624*, 46–65. [CrossRef]
9. Fabris, A.; Katona, L.; Reed, G.; Keeping, T.; Gordon, G.; Gouthas, G.; Swain, G. Mapping the Punt Hill IOCG system using geophysical, geochemical and spectral methods—An integrated approach. In Proceedings of the Australian Society of Exploration Geophysicists ASEG Conference, 25th, Adelaide, Australia, 20 August 2016; pp. 1–9. [CrossRef]
10. Sun, J.; Li, Y. Multidomain petrophysically constrained inversion and geology differentiation using guided fuzzy c-means clustering. *Geophysics* **2015**, *80*, ID1–ID18. [CrossRef]
11. Sun, J.; Li, Y. Joint inversion of multiple geophysical and petrophysical data using generalized fuzzy clustering algorithms. *Geophys. J. Int.* **2017**, *208*, 1201–1216. [CrossRef]
12. Melo, A.T.; Sun, J.; Li, Y. Geophysical inversions applied to 3d geology characterization of an iron oxide copper-gold deposit in Brazil. *Geophysics* **2017**, *82*, K1–K13. [CrossRef]
13. Melo, A.T. Integrated Quantitative Interpretation of Multiple Geophysical Data for Geology Differentiation. PhD Thesis, Colorado School of Mines, Golden, CO, USA, 2018.
14. Costa, I.S.L.; Tavares, F.M.; Oliveira, J.K.M. Predictive lithological mapping through machine learning methods: A case study in the Cinzento lineament, Carajás province, Brazil. *J. Geol. Surv. Braz.* **2019**, *2*, 26–36. [CrossRef]
15. Melo, A.T.; Li, Y.; Hitzman, M. Is there hidden potential in Carajás? Insights through the geophysical signature of Cristalino deposit. *Ore Geol. Rev.* **2020**, *126*, 1–13. [CrossRef]
16. Martins, T.F.; Seoane, J.C.S.; Tavares, F.M. Cu-Au exploration target generation in the eastern Carajás Mineral Province using random forest and multi-class index overlay mapping. *J. South Am. Earth Sci.* **2022**, *116*, 103790. [CrossRef]
17. Hitzman, M.W.; Oreskes, N.; Einaudi, M.T. Geological characteristics and tectonic setting of Proterozoic iron oxide (Cu-U-Au-REE) deposits. *Precambrian Res.* **1992**, *58*, 241–287. [CrossRef]
18. Oreskes, N.; Einaudi, M.T. Origin of rare earth element enriched hematite breccias at the Olympic Dam Cu-U-Au-Ag deposit, Roxby Downs, South Australia. *Econ. Geol.* **1990**, *85*, 1–28. [CrossRef]
19. Oreskes, N.; Einaudi, M.T. Origin of hydrothermal fluids at Olympic Dam: Preliminary results from fluid inclusion and stable isotopes. *Econ. Geol.* **1992**, *87*, 64–90. [CrossRef]
20. Williams, P.J.; Barton, M.D.; Johnson, D.A.; Fontboté, L.; Haller, A.; Mark, G.; Oliver, N.H.S.; Marschik, R. Iron Oxide Copper-Gold Deposits: Geology, Space-Time Distribution, and Possible Modes of Origin. In *Economic Geology*; Society of Economic Geologists: Littleton, CO, USA, 2005; 100th Anniversary Volume, pp. 371–405. [CrossRef]
21. Groves, D.I.P.; Bierlein, F.P.; Meinert, L.D.; Hitzman, M.W. Iron oxide copper-gold (IOCG) deposits through Earth history; implications for origin, lithospheric setting, and distinction from other epigenetic iron oxide deposits. *Econ. Geol.* **2010**, *105*, 641–654. [CrossRef]
22. Barton, M.D. Iron Oxide(-Cu-Au-REE-P-Ag-U-Co) Systems. In *Treatise on Geochemistry*, 2nd ed.; Holland, H.D., Turekian, K.K., Eds.; Elsevier: Amsterdam, The Netherlands, 2014; Volume 13, pp. 515–541. [CrossRef]
23. Logan, L.; Andersson, J.B.H.; Whitehouse, M.J.; Martinsson, O.; Bauer, T.E. Energy Drive for the Kiruna Mining District Mineral System(s): Insights from U-Pb Zircon Geochronology. *Minerals* **2022**, *12*, 875. [CrossRef]
24. Skirrow, R.G. Iron oxide copper-gold (IOCG) deposits—A review (part 1): Settings, mineralogy, ore geochemistry and classification. *Ore Geol. Rev.* **2022**, *140*, 104569. [CrossRef]
25. Mougeot, R.; Respaut, J.P.; Briqueu, L.; Ledru, P.; Milesi, J.P.; Lerouge, C.; Marcoux, E.; Huhn, S.B.; Macambira, M.J.B. Isotope Geochemistry Constrains for Cu, Au Mineralization and Evolution of the Carajas Province (Para, Brazil). In Proceedings of the 39th Congresso Brasileiro de Geologia, Salvador, Brazil, 1–6 September 1996; Volume 7, pp. 321–324.
26. Monteiro, L.V.S.; Xavier, R.P.; Carvalho, E.R.; Hitzman, M.W.; Johnson, C.A.; Filho, C.R.S.; Torresi, I. Spatial and temporal zoning of hydrothermal alteration and mineralization in the Sossego iron oxide-copper-gold deposit, Carajás Mineral Province, Brazil: Paragenesis and stable isotope constraints. *Miner. Depos.* **2008**, *43*, 129–159. [CrossRef]

27. Xavier, R.P.; Monteiro, L.V.S.; Moreto, C.P.N.; Pestilho, A.L.S.; Melo, G.H.C.; Silva, M.A.D.; Aires, B.; Ribeiro, C.; Silva, F.H.F. The iron oxide copper-gold systems of the Carajás Mineral Province, Brazil. In *Geology and Genesis of Major Copper Deposits and Districts of the World*, 1st ed.; Hedenquist, J.W., Harris, M., Camus, F., Eds.; Society of Economic Geologists: Littleton, CO, USA, 2012; Special Publication Number 16; pp. 433–454. [CrossRef]
28. Campo-Rodríguez, Y.T.; Schutesky, M.E.; Oliveira, C.G.; Whitehouse, M.J. Unveiling the polyphasic evolution of the Neoarchean IOCG Salobo deposit, Carajás Mineral Province, Brazil: Insights from magnetite trace elements and sulfur isotopes. *Ore Geol. Rev.* **2022**, *140*, 104572. [CrossRef]
29. Huang, X.W.; Beaudoin, G.; Yang, Y. A HR-TEM study on two generations of magnetite from the Alemao IOCG deposit, Carajás, Brazil: Implication for Fe-Cu mineralization. *Ore Geol. Rev.* **2022**, *146*, 104934. [CrossRef]
30. Corriveau, L.; Mumin, A.H.; Setterfield, T. IOCG environments in Canada: Characteristics, geological vectors to ore and challenges. In *Hydrothermal Iron Oxide Copper-Gold and Related Deposits: A Global Perspective*; Porter, T.M., Ed.; PGC Publishing: Adelaide, Australia, 2010; Volume 4, pp. 311–344.
31. Corriveau, L.; Williams, P.J.; Mumin, A.H. Alteration vectors to IOCG mineralization: From uncharted terranes to deposits. In *Exploring for Iron Oxide Copper-Gold Deposits: Canada and Global Analogues*; Corriveau, L., Mumin, A.H., Eds.; Short Course Notes; Geological Association of Canada: St. John's, NL, Canada, 2010; Volume 20, pp. 89–110.
32. Corriveau, L.; Montreuil, J.F.; Potter, E.G. Alteration facies linkages among iron oxide copper-gold, iron oxide-apatite, and affiliated deposits in the Great Bear magmatic zone, Northwest Territories, Canada. *Econ. Geol.* **2016**, *111*, 2045–2072. [CrossRef]
33. Santos, J.O.S.; Hartmann, L.A.; Gaudette, H.E.; Groves, D.I.; McNaughton, N.J.; Fletcher, I.R. A new understanding of the provinces of the Amazon Craton based on integration of field mapping and U-Pb and Sm-Nd geochronology. *Gondwana Res.* **2000**, *3*, 453–488. [CrossRef]
34. Hirata, W.K.; Rigon, J.C.; Cordeiro, A.A.C.; Meireles, E.M. Geologia Regional da Província Mineral de Carajás. In Proceedings of the 1° Simpósio de Geologia da Amazônia SBG, Belém, Brazil, 25 May 1982; pp. 100–108.
35. DOCEGEO. Revisão Litoestratigráfica da Província Mineral de Carajás. In Proceedings of the 35° Congresso Brasileiro de Geologia SBG, Belém, Brazil, 1 November 1988; pp. 11–56.
36. Araújo, O.J.B.; Maia, R.G.N. *Projeto Especial Mapas de Recursos Minerais, de Solos e de Vegetação para a Área do Programa Grande Carajás, Subprojeto Recursos Minerais, Folha SB.22-Z-A Serra dos Carajás-Estado do Pará*; DNPM/CPRM: Brasília, Brazil, 1991; 136p.
37. Barros, C.E.M.; Barbey, P. A importância da granitogênese tardi-arqueana (2.5 Ga.) na evolução tectono-metamórfica da Província Mineral de Carajás—O Complexo Granítico Estrela e sua auréola de contato. *Rev. Bras. Geociênc.* **1998**, *28*, 513–522. [CrossRef]
38. Vasquez, M.L.; Sousa, C.S.; Carvalho, J.M.A. Mapa Geológico e de Recursos Minerais do Estado do Pará, Escala 1:1.000.000, Programa Geologia do Brasil (PGB). Serviço Geológico do Brasil: Brasília, Brazil, 2008.
39. Wirth, K.R.; Gibbs, A.K.; Olszewski, W.J. U-Pb ages of zircons from the Grão-Pará Group and Serra dos Carajás Granite, Pará, Brazil. *Rev. Bras. Geociênc.* **1986**, *16*, 195–200. [CrossRef]
40. Lindenmayer, Z.G. Salobo Sequence, Carajás, Brazil: Geology, Geochemistry and Metamorphism. Ph.D. Thesis, University of Western Ontario, London, OT, Canada, 1990.
41. Lindenmayer, Z.G.; Teixeira, J.B.G. Ore Genesis at the Salobo Copper Deposit, Serra dos Carajás. In *Base Metal Deposits of Brazil*; Silva, M.G., Misi, A., Eds.; MME/CPRM/DNPM: Brasília, Brazil, 1999; pp. 33–43.
42. Vale, S.A. *Projeto Furnas, Relatório Final de Geologia: Internal Technical Report*; Vale: Parauapebas, Brazil, 2012.
43. Leão-Santos, M.H.; Li, Y.; Moraes, R.A.V. Application of 3D magnetic amplitude inversion to Fe oxide-Cu-Au deposits at low magnetic latitudes: A case study from Carajás Mineral Province, Brazil. *Geophysics* **2015**, *80*, B13–B22. [CrossRef]
44. Li, Y.; Oldenburg, D.W. 3-D inversion of magnetic data. *Geophysics* **1996**, *61*, 394–408. [CrossRef]
45. Telford, W.M.; Geldart, L.P.; Sheriff, R.E. *Applied Geophysics*, 2nd ed.; Cambridge University Press: Cambridge, UK, 1990; 770 p.
46. Seequent, Geosoft Oasis Montaj Software, 3D Kriging GX. Available online: https://www.seequent.com/ (accessed on 15 July 2021).